Faculty of Engineering of the University of Porto

School of Medicine and Biomedical Sciences

Electrochemical miRNA-based biosensor for the diagnosis of Alzheimer's Disease

Raquel Filipa Lemos Pereira

Dissertation performed as part of the
Masters in Bioengineering – Molecular Bioengineering

Supervisor: Felismina Moreira, PhD (BioMark, ISEP)
Co-supervisors: Sofia Santos, PhD (nBTT, i3S)
Ana Paula Pêgo, PhD (nBTT, i3S)

15th September, 2022

© Raquel Pereira, 2022

Abstract

The aim of the work herein presented is to develop an electrochemical miRNA-based biosensor for the diagnosis of Alzheimer's Disease (AD).

AD is the most common type of dementia and a prominent cause of death and disability in the elderly. This disease is associated with an enormous socioeconomic expense, which is projected to keep increasing as the life expectancy of the population increases. Unfortunately, at present, there are no curative treatments for this disease. The treatment is focused on a multidisciplinary approach, where medication is used to slow down the progression of the disease or to mask its symptoms. The earliest the diagnosis is made, the better the prognosis of the patients. Thus, early-stage diagnosis becomes critical in AD patient care. However, currently available diagnostic tools are expensive and invasive. To circumvent this problem, it is imperative to design new, less-expensive, and less-invasive tools for AD diagnosis. Recently, circulating miRNAs have attracted great interest as AD biomarkers because their expression levels are affected (in tissue and in blood) alongside with disease progression. microRNA-34a (miR-34a), in particular, has been consistently reported as a reliable AD blood biomarker. On the other hand, electrochemical biosensors have been widely used as point-of-care (POC) platforms for the detection of blood analytes. Combining the advantages of miRNAs and electrochemical biosensors with the need for new AD diagnostic tools, the idea of designing a miR-34a-based biosensor for the detection of AD was born.

Many strategies were explored to attempt to develop a sensor that was able to detect miR-34a. The final biosensing device here presented is based on the modification of a commercial carbon screen-printed electrode (C-SPE) with nanostructured gold and a complementary anti-miR-34a oligonucleotide probe. The C-SPE provides the inexpensiveness and flexibility of a commercially available platform; the nanostructured gold provides a larger surface area for modification and an improvement of the electrochemical properties of the C-SPEs; and the anti-miR-34a oligonucleotide probe provides specificity to the sensor.

Overall, this biosensor performed well and was able to meet the goal of the project. It demonstrated good target affinity and allowed miR-34a detection within a linearity range of 100 pM to 1 μM, both in buffer and in serum. Moreover, the biosensor's response remained unaffected in the presence of two potentially interfering serum compounds (miR-107 and creatinine), indicating that it is selective for the target miRNA. As a proof of concept, the biosensor proved to be able to detect the presence of miR-34a in the cell media of the retinoic acid-stimulated SH-SY5Y neuronal cell line, which is commonly used as an AD cellular model. Furthermore, the sensor was able to detect an increase in extracellular miR-34a as a result of the exposure of this cell line to a neurotoxicant stimulus (6-hydroxidopamine, 6-OHDA).

In conclusion, the proposed biosensor represents a starting point for the introduction of a low-cost, minimally invasive sensor for AD diagnosis in clinical practice. This sensor holds great promise for early AD diagnosis and opens the possibility for pre-symptomatic diagnosis, halting disease progression even before the onset of the first symptoms.

Acknowledgments

Esta dissertação marca o final de um semestre de muito trabalho e dedicação.

Em primeiro lugar, quero agradecer à minha orientadora e coorientadoras, Doutora Felismina Moreira, Doutora Sofia Santos e Doutora Ana Paula Pêgo, por terem possibilitado esta experiência. Um especial obrigada à Doutora Felismina e à Doutora Sofia por todo o apoio e pelas correções feitas a este trabalho.

Em segundo lugar, quero agradecer ao pessoal do BioMark e do grupo nBTT por me terem acolhido de forma tão carinhosa e gentil no vosso espaço. Em particular, quero agradecer à Doutora Felismina e à Doutora Ana Paula por terem posto à disposição todos os recursos dos seus grupos. Quero também deixar um especial agradecimento à Daniela Oliveira por ter supervisionado o meu trabalho laboratorial e por me ter ajudado a solucionar tantos problemas.

Em terceiro lugar, não posso deixar de agradecer aos que partilharam comigo esta jornada de aventura e crescimento. Aos suspeitos do costume, Ana, Diogo, Guilherme, Inês, Nuno e Rafa, obrigada por estarem ao meu lado e por serem a minha casa fora de casa.

Finalmente, quero agradecer à minha família todo o apoio demonstrado. Mãe e pai agradeço-vos do fundo do meu coração por terem incentivado os meus sonhos e por terem acreditado que um dia a vossa menina podia tornar-se uma engenheira.

Funding

The work presented in this dissertation was financially supported by:

- Project NORTE-01-0145-FEDER-000008 and NORTE-01-0145-FEDER-000012, supported by Norte Portugal Regional Operational Programme (NORTE 2020), under the PORTUGAL 2020 Partnership Agreement, through the European Regional Development Fund (ERDF) and FEDER - Fundo Europeu de Desenvolvimento Regional funds through the COMPETE 2020-Operacional Programme for Competitiveness and Internationalisation (POCI), Portugal 2020;
- Portuguese funds through FCT/MCTES in the framework of the project "Institute for Research and Innovation in Health Sciences" (POCI-01-0145-FEDER-007274);
- National Funds through FCT – Fundação para a Ciência e a Tecnologia (iDNArT - PTDC/NAN-MAT/30898/2017) and under the Norma Transitória – DL 57/2016/CP1360/CT0013;
- Project "2IQBIONEURO – Promotion of a research and development network in biological chemistry for the diagnosis and treatment of neurological diseases" (reference: 0624_2IQBIONEURO_6_E), co-funded by the INTERREG Program V-A POCTEP through the European fund for Regional Development (FEDER).

The author also acknowledges the support of the i3S Scientific Platform Bioimaging, member of the national infrastructure PPBI - Portuguese Platform of Bioimaging (PPBI-POCI-01-0145-FEDER-022122).

The development and testing of the biosensor was carried out in BioMark, Instituto Superior de Engenharia do Porto (ISEP). The cellular studies were carried out in the NanoBiomaterials for Targeted Therapies group (nBTT) group, at Instituto de Investigação e Inovação em Saúde (i3S).

Index

List of figures

List of tables

Abbreviations and Symbols

List of abbreviations

AD	Alzheimer's Disease
Ago2	Argonaute 2
3-MPA	3-mercaptopropionic acid
6-OHDA	6-hydroxydopamine
ACh	Acetylcholine
AChEIs	Acetylcholinesterase inhibitors
Ag	Silver
ApoE	Apolipoprotein E
APP	Amyloid precursor protein
Asn	L-asparagine
Au	Gold
CA	Chronoamperometry
CE	Counter electrode
cimiRNA	Circulating miRNA
CNS	Central nervous system
CSF	Cerebrospinal fluid
C-SPE	Carbon screen-printed electrode
CT	Computed tomography
CV	Cyclic voltammetry
DAPI	4′,6-diamidino-2-phenylindole
DEPC	Diethyl pyrocarbonate
DIFF_0	SH-SY5Y cells cultured in Differentiation Medium
DIFF_100	SH-SY5Y cells cultured in Differentiation Medium supplemented with 100 μM 6-OHDA
DIFF_50	SH-SY5Y cells cultured in Differentiation Medium supplemented with 50 μM 6-OHDA
Differentiation Medium	Low-glucose DMEM supplemented with 1% FBS, 0.1% gentamicin sulphate 50 mg/mL and 10 μM RA
DMEM	Dulbecco's Modified Eagle Medium
DNA	Desoxyribonucleic acid
EDAC	1-ethyl-3-(3-dimethylaminopropyl)carbodiimide
EIS	Electrochemical impedance spectroscopy
FBS	Foetal bovine serum
FDA	United States' Food and Drug Administration

GCE	Glassy carbon electrode
HDL	High-density lipoproteins
HEPES	4-(2-hydroxyethyl)-1-piperazineethanesulfonic acid
Hybridization Buffer, pH=7.4	Phosphate buffer with 50 mM $MgCl_2$ and 150 mM NaCl, at pH=7.4
Hybridization Buffer, pH=8	Phosphate buffer with 5 mM $MgCl_2$ and 150 mM NaCl, at pH=8
i3S	Instituto de Investigação e Inovação em Saúde
iPSCs	Induced pluripotent stem cells
ISEP	Instituto Superior de Engenharia do Porto
LOD	Limit of detection
miR/miRNA	microRNA
MPP+	1-methyl-4-phenylpyridinium
MPTP	1-methyl-4-phenyl-1,2,3,6-tetrahydropyridine
MRI	Magnetic resonance imaging
mRNA	Messenger RNA
nBTT	NanoBiomaterials for Targeted Therapies group
NFTs	Neurofibrillary tangles
NHS	N-hydroxysuccinimide
NMDA	N-methyl d-aspartate
Non-DIFF	SH-SY5Y cells cultured in Non-Differentiation Medium
Non-differentiation Medium	DMEM (1x) + GlutaMAX™-I supplemented with 15% FBS and 0.1% gentamicin sulphate 50 mg/mL
NP-Au	Nanoporous gold
NPs	Nanoparticles
OS	Oxidative stress
PBS	Phosphate-buffered saline
PCR	Polymerase chain reaction
PET	Positron emission tomography
PGEs	Pencil graphite electrodes
Pl	Palladium
POC	Point-of-care
Pt	Platinum
R^2	Coefficient of determination
RA	Retinoic acid
RE	Reference electrode
REST	Repressor element-1 silencing transcription factor
RISC	RNA-induced silencing complex
RNA	Ribonucleic acid
ROS	Reactive oxygen species

RT	Room temperature
SAMs	Self-assembled monolayers
SEM	Scanning electron microscopy
SIRT1	Sirtuin1
SPEs	Screen-printed electrodes
STX1A	Syntaxin 1A
SWV	Square-wave voltammetry
SYT1	Synaptotagmin 1
US	United States of America
UTRs	Untranslated regions
WE	Working electrode

List of symbols

C_{dl}	Double layer capacitance
E	Potential
E_f	Final potential
E_p	Peak potential
E_s	Start potential
I	Current
I_{for}	Forward current
I_{max}	Maximum peak height
I_{net}	Net current
I_p	Peak current
I_{rev}	Reverse current
R_{ct}	Charge transfer resistance
R_s *or* R_Ω	Resistance of the electrolyte
Z	Impedance
$Z_{imaginary}$ *or* Z''	Imaginary part of the impedance
Z_{real} *or* Z'	Real part of the impedance
ΔE_p	Peak-to-peak separation

Chapter 1

Introduction

This chapter provides a theoretical introduction to the work herein presented. It starts with an overview of the target disease – Alzheimer's Disease (AD), continues with a review of the evidence linking miR-34a to AD, and ends with a compilation of the current state of the art in nanostructured miRNA-based biosensors and their utility in disease diagnosis.

Throughout this chapter, the reader is made aware of the socioeconomic impact of AD, the pressing need for new, less-invasive diagnostic methods for this disease, and the underexplored potential of miRNA biomarkers. Likewise, the reader is introduced to the distinctive advantages of electrochemical biosensors and to some key electrochemical concepts necessary to later discuss the obtained results.

Altogether, this chapter lays the theoretical foundation for understanding the importance of this work and the topics herein covered.

1.1 - Alzheimer's Disease

Historical background

AD is a type of dementia named by Emil Kraepelin, in 1910, in his 8th edition Handbook of Psychiatry [1]–[3]. This condition was named after Alois Alzheimer, a German psychiatrist who firstly reported the presence of amyloid plaques and neurofibrillary tangles as well as massive loss of neurons in the brain of a patient who died of early onset dementia [2]–[5].

In his handbook, Kraepelin reported AD as a new disease, distinct from the historically known senile dementia. The idea that AD was a rare psychiatric and neurological disorder, confined to young patients, persisted for almost 50 years after Alzheimer presented his work. In fact, up until the 1970's, senile and presenile disorders were considered separate entities [2]. This paradigm fundamentally shifted in 1976, when Robert Katzman published a study gathering evidence that senile and presenile dementia had the same histopathological hallmarks [3]. From then onwards, clinicopathological studies have shown that AD and senile dementia are simply different stages of the same disease (AD) [2], transforming AD from a rare event to a major public health concern [3].

Socioeconomic landscape

AD is the most common type of dementia and accounts for 60 to 80% of all dementia cases [6]–[8]. Furthermore, AD is a prominent cause of death, morbidity, dependence, and disability in the elderly, for which there are no effective curative or preventative treatments available [7], [9]. In fact, in 2019, over 120 thousand people died from this disease in the United States of America (US), making AD the sixth-leading cause of death in this country [10].

Currently, the prevalence of AD in middle-aged people (under 65 years) is estimated at 5% [9], [11]. However, this percentage rises to 30% in elders over 85 years [12]. Overall, around 50 million people suffer from AD worldwide and this number is forecastable to increase as the lifespan keeps growing [7], [13]. By 2030, AD prevalence in the world is expected to reach over 75 million people [7] and to rise to 130 to 135 million people, by 2050 [7], [11], [14]. Perhaps due to their higher life-expectancy [9], women are more afflicted by this disease than men [8], [15].

The costs associated with medication, caretaking and diagnosis of AD patients have a significant impact not only on the patients and their caregivers, but also on their communities and societies, creating a tremendous economic burden around this condition [6], [9], [16]. In the US alone, $305 billion were spent on the healthcare (including long-term care and hospice) of dementia patients in 2020. This annual expenditure is projected to increase nearly 4-fold in the next thirty years (totalling over $1.1 trillion by 2050) [8], due to the continuous aging of the population [17]. This expense is even greater when the societal impact of the disease is considered. When indirect costs (such as the loss of productivity experienced by the patient and their caregiver, or the healthcare-related costs associated with caregiver burden) are included in the calculations [9], [16], the annual societal cost of dementia rises to an impressive amount of $818 billion in the US, which is equivalent to 1.1% of their global gross domestic product [16].

Symptomatology

AD is a complex and multifactorial age-related disease [7], [18] characterized by the progressive loss of neurons and synapses in the brain – neurodegeneration – which results in loss of cognitive function and cholinergic deficits [18]–[22]. The symptoms vary from patient to patient but collectively lead to a decline, and eventual loss, of self-sufficiency [23].

This disease is divided in three stages: preclinical, prodromal and dementia [20], [24]. The preclinical stage, often called preclinical AD, precedes all symptoms; it is a stage of slow and asymptomatic development (often lasting for decades) where the biological, tissue and cellular changes, that lead to pathology down the line, occur. The prodromal stage is characterized by mild cognitive impairment [24]. It often starts with episodes of forgetfulness and confusion, which then evolve to severe difficulties with speech/language, cognition, motor control, and other functions. The last stage – dementia – leads to irreversible disruptions of visual and visuospatial perception, behavioural alterations, self-isolation, worsening of cognitive and memory performance, hallucinations, and loss of autonomy [19], [20], [22]. The progression of the severity of patients' symptoms over time is schematically represented on Figure 1 [10].

Patients with the dementia also become more prone to comorbidities, such as diabetes mellitus, hypertension, and cardiovascular disease [9]. Generally, after symptom onset, patients experience a decline in brain capacity and autonomy until their death, which on average occurs 8.5 years after symptom presentation [8], [22].

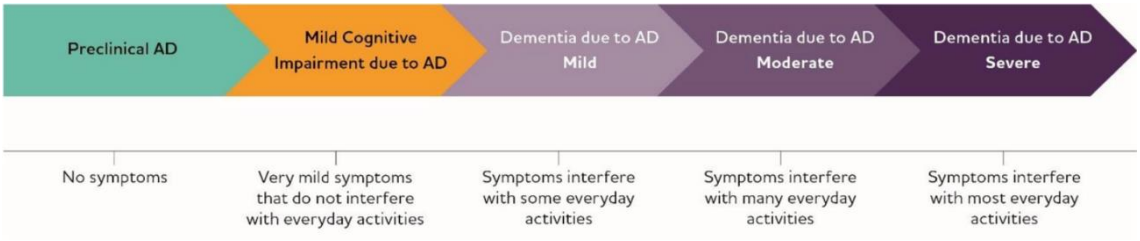

Figure 1 – AD symptom progression. Extracted from *Alzheimer's Association, 2021* [10].
Note: the length of the arrows is not representative of the duration of the stage.

Pathophysiology

Despite the exponential amount of research conducted on dementia in the past 20 years [9], the causes and molecular mechanisms behind AD remain unclear [7], [20], [22], [25]. Most cases of AD appear to have an idiopathic and sporadic origin [26], for which the best-known risk factors are mutations in Apolipoprotein E (ApoE) [23]. However, a small percentage of cases (less than 0.5%) arise from hereditary, autosomal-dominant mutations in amyloid precursor protein (APP), presenilin 1 or presenilin 2 proteins – familial AD [22], [23]. Typically, familial AD manifests early (between 30 and 50 years of age) whereas sporadic AD, also referred to as late-onset AD, typically manifests later on in life (past the age of 70) [17], [22].

The abnormalities most commonly associated with AD pathology are (i) the accumulation of misfolded Aß protein (as plaques or oligomers) outside of the neurons (extracellularly) and (ii) the formation of neurofibrillary tangles (NFTs) of tau proteins inside the neuronal cells [8], [14], [21]–[23], [27], [28]. Aß amyloidosis is thought to interfere with synaptic communication between neurons, whereas tau tangles are thought to block the transport of nutrients and other important factors within the neurons. Moreover, both abnormalities can trigger the microglia, inducing inflammation and abnormal glucose metabolism [8]. It is hypothesized that Aß amyloidosis initiates as soon as AD pathogenesis starts, whilst NFT formation occurs further down the disease progression continuum [22]. However, it is equally likely that both processes initiate simultaneously and reinforce each other's toxic effects [13].

Aß amyloidosis results from the aggregation of the insoluble Aß-42 isoform. The Aß-42 isoform has two more amino acids (isoleucine and alanine) than the normal Aß-40 isoform, which reduce its solubility and facilitate aggregation/formation of plaques. Aß-42 formation is the aftermath of an abnormal cleavage of the membrane-bound Aß precursor protein by γ-secretase. This can occur for several reasons, including mutations in the APP, presenilin 1/2 or ApoE4 genes [15], [22]. Even though the amyloid deposition pattern may vary, it usually starts in the isocortex and later extends to subcortical structures. Sometimes it also reaches the entorhinal cortex and the hippocampal formations, howbeit to a lesser extent [22].

NFTs result from the deposition of paired helical filaments of hyperphosphorylated tau proteins in the cytosol [4], [15], [22]. Tau proteins bind to the microtubules through the phosphorylation of their serine/threonine residues [15]. This binding has two function: (i) it facilitates neuronal transport [13] and (ii) it regulates the stabilization and polymerization of the microtubule assembly, necessary to stabilize growing axons and, thus, ensure proper neuronal development and function [13], [15]. When tau proteins are hyperphosphorylated they lose their affinity to the microtubules and get deposited in the cytosol, eventually leading to the formation of NFTs. In turn, microtubule dissociation leads to loss of axonal transport and synaptic plasticity [4]. Hyperphosphorylation of tau proteins has mainly been attributed to a mutation in the tau genes or a dysregulation of the kinases and phosphatases that regulate the

phosphorylation state of tau proteins [15]. In contrast with Aß amyloidosis, tau pathology usually begins in the entorhinal cortex and hippocampus, and then spreads to the associative isocortex. The primary motor, visual and sensory regions tend to remain unaffected [22].

To simplify the communication of the pathophysiological alterations related to Aß amyloidosis and tau NFTs, Braak and Braak created, in 1991, a categorization system – the Braak and Braak (or Braak, for short) system – based on the mapping of these changes. The movement of the Aß amyloid plaques was divided in three categories (Stage 1, Stage 2, and Stage 3), whereas the movement of the NFTs was divided in six categories (I, II, III, IV, V, and VI). These two categories can be corelated to each other as well as to the status of disease propagation, as shown in the scheme on Figure 2 [29].

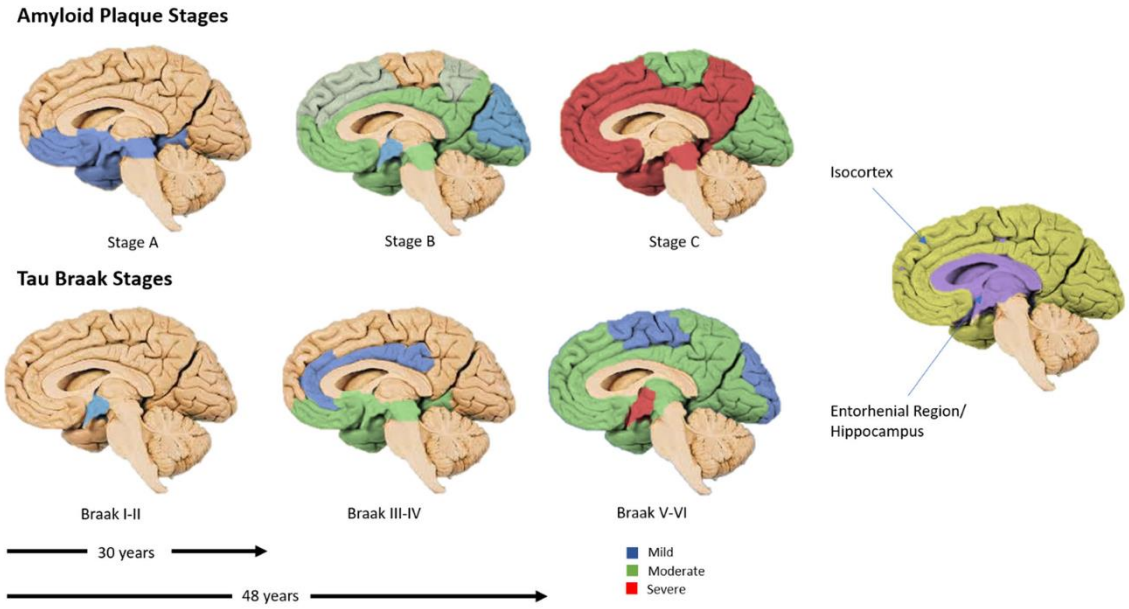

Figure 2 – Spatiotemporal distribution of the Aß amyloidosis and the tau NFTs through the Braak system stages. Mild, moderate, and severe refer to the density of amyloid/ tau protein. Extracted from *Swarbrick et al., 2019* [29].

The transentorhinal stages I–II correspond to clinically silent cases, the limbic stages III–IV to incipient AD and, finally, the neocortical stages V–VI to fully developed AD [30]. Besides these factors, evidence suggests that the pathophysiology of AD might also be associated with oxidative stress (OS), iron dyshomeostasis, aberrant cell cycle entry, gliosis, and/or single-nucleotide polymorphisms, particularly in the ApoE gene [8], [15], [17], [18], [20], [28]. Post-mortem brain samples, biological fluid samples, animal models and induced pluripotent stem cells (iPSCs) have shown that OS is an early-stage event in AD pathology. Additionally, animal models and iPSCs indicate that OS elevation occurs at the same time (or even prior) to Aß and tau pathology, which is why, recently, OS has been appointed as the main pathomechanism of AD [31]. In any case, the cognitive deficits observed in AD patients are the result of progressive neuronal loss and its subsequent neurotransmitter imbalance [13].

Treatment

As previously mentioned, at present, there are no effective curative treatments for AD [17], [32]. Treatments for AD provide only a modest and temporary cognitive benefit, and do

not alter the natural progression of the disease [17]. Furthermore, symptoms often arise at a rather advanced disease stage, where treatments are ineffective [4].

Most commercially available AD treatments attempt to correct the neurotransmitter imbalance of the disease [13], and can be split into two categories: acetylcholinesterase inhibitors (AChEIs) and antagonists to N-methyl d-aspartate (NMDA) [1], [13]. AChEIs can be reversible, irreversible, or pseudo-reversible [1]; they act by blocking acetylcholine (ACh) degradation by cholinesterase enzymes, thus increasing the availability of ACh (a neurotransmitter) in the synaptic cleft. NMDA antagonists work by preventing the overactivation of NMDA receptors and, hence, Ca^{2+} influx to the neurons. This blocks Ca^{2+} mediated cellular death and synaptic dysfunction, and ameliorates the effects of glutamate-mediated excitotoxicity [1], [13], [33].

Currently, the only Federal Drug Administration (FDA) approved medications of these pharmacological classes are donepezil, galantamine, rivastigmine (AChEIs) and memantine (NMDA antagonist) [1], [5], [13]. As previously mentioned, although effective at treating AD symptoms, neither of these drugs cures or prevents the disease [1]. Moreover, treatment with AChEIs should be initiated as soon as possible after diagnosis, since patients who start the medication later on show a more rapid cognitive decline [13].

Recently, a new hope for treating AD has emerged with the FDA approval of aducanumab (marketed as Aduhelm), in 2021. Aducanumab is an Aß-directed antibody which decreases the amount of Aß peptides. This therapy may also be used for secondary prevention in pre-symptomatic individuals with cerebral Aß deposits [33]. However, it is worth noting that this drug was approved under the accelerated approval pathway [34], and that the approval process generated great controversy since phase III trials failed to demonstrate improved cognition as a primary outcome [33]. Therefore, aducanumab can still be withdrawn from the market if the sponsor fails to verify clinical benefit in a post-approval trial [34].

Nowadays, a multifactorial management of AD is preferred. This approach combines the use of medication with behavioural techniques and caregiver support. Behavioural techniques include exercise therapy, cognitive behavioural therapy, consistency and simplification of the environment, implementation of established routines, as well as communicative strategies. On the other hand, caregiver support relies on the psychoeducation of caregivers (educating them on the expectable effects of AD on the cognition, behaviour, and function of the patient) and on the promotion of support networks and rest periods for the caregivers. In addition to the aforementioned pharmacological treatments, the removal of unnecessary medication and/or the administration of antipsychotics and antidepressants may also be considered as part of the treatment of AD patients [13].

Ultimately, due to the lack of effective curative treatments for AD [17], [32], the earlier the diagnosis can be made (and the less developed the disease is at this time), the higher the changes of successfully treating the patient [29]. Furthermore, since the onset of the biological alterations conducing to AD pathology can begin decades prior to symptom appearance, it is urgent to identify novel early-stage biomarkers for this disease [35].

In vitro models

In the past 40 years, many cellular models have been developed to try to better understand the pathophysiology of AD as well as attempt to combat it [17]. For instance, plenty of the information known about APP processing and γ-secretase functions came from cell culture

experiments [5]. Likewise, many of the effects of Aß were studied using cultured human and rodent neuronal cells [17].

There are several types of models that can be used to study neurodegenerative diseases, including AD. Primary cultures of rat hippocampal and cortical neuronal cells were introduced in 1976 by Banker and Cowan and are nowadays one of the most used models to study AD-like cellular features. Human embryonic stem cells and iPSCs are currently also widely used to study AD pathophysiology and neurodegeneration [33], [36]. Human iPSCs were introduced in 2007, and can be differentiated into several cell types, including neurons [17], [36]. Immortalized cell lines can also be differentiated into neurons and are highly attractive for the study of the central nervous system (CNS). Some of the most used immortalized cell lines include PC12 (isolated from a tumour of a rat adrenal medulla), N2a (derived from a mouse neural crest) and human neuroblastoma cell lines, such as the SH-SY5Y cell line [36]. Lastly, 3D models and co-cultures are gaining traction as they more closely resemble the *in vivo* conditions and better mimic the interdependence between individual neurons and their microenvironment.

Immortalized cell lines are often used as a starting point for CNS research as they are relatively simple to handle, commercially available, inexpensive and can be continuously proliferated [33]. Moreover, some of these cells can be differentiated into neurite bearing cells that express neuronal markers, such as ß-tubulin III and neurofilament [36]. The human neuroblastoma SH-SY5Y cell line is one of the commonly used immortalized cell lines for this purpose [33]. This line was subcloned three times from SK-N-SH cells, obtained from the bone marrow of a child suffering from sympathetic adrenergic ganglial neuroblastoma (a rare type of nerve cell cancer) [33], [37]. The SH-SY5Y line is highly useful for neuroscience, including neurodegeneration studies, which are extremely relevant in AD [37]. Unlike other cell lines, undifferentiated SH-SY5Y cells present a correct neurite structure and express immature neuronal biomarkers [33]. They exhibit neuronal marker enzyme activity (tyrosine and dopamine-ß-hydroxylases) and specific uptake of norepinephrine. SH-SY5Y cells also express neurofilament proteins and opioid, muscarinic, and nerve growth factor receptors [38], [39]. Moreover, these cells can be differentiated into a neuronal-like cell population. During differentiation, the cell cycle synchronizes, the cells stop dividing and a constant population of cells with a functional mature neuronal phenotype is produced [40]. Depending on the agent used for differentiation induction, different neuronal phenotypes and biochemical changes are produced. For example, under the induction of retinoic acid (RA), SH-SY5Y cells can differentiate into a cholinergic neuronal phenotype [40], [41], relevant for AD research [37]. Exposure to RA also increases the susceptibility of SH-SY5Y cells to neurotoxic agents [41], which can be used to promote cellular death and mimic the process of neurodegeneration. Aß oligomers are often added to simulate AD, whereas 6-hydroxydopamine (6-OHDA), 1-methyl-4-phenyl-1,2,3,6-tetrahydropyridine (MPTP), or rotenone are added to simulate Parkinson's Disease (PD) [33], [42]. Notably, exposure of SH-SY5Y cells to 6-OHDA or 1-methyl-4-phenylpyridinium (MPP+, a precursor of MPTP) has also been shown to increase the expression and secretion of miR-34a, a promising new biomarker for AD [43]–[45].

Diagnosis

Up until 2011, AD diagnosis could only be confirmed post-mortem, after autopsy of the patient's brain. However, currently, AD diagnosis is done premortem [8], via neuroimaging - employing techniques such as magnetic resonance imaging (MRI), computed tomography (CT) or positron emission tomography (PET) scans -, interviews with relatives, cognitive tests,

and/or analysis of bodily fluids [12], [15], [20], [22]. Since 2018, the National Institute on Aging and Alzheimer's Association implemented the Alzheimer's Diagnostic Framework to diagnose AD based on biomarker criteria [8], [22]. This originated the A/T/N classification scheme which classifies patients based on: (A) the alteration/ deposition of Aß proteins in the brain, (T) the presence of hyperphosphorylated tau proteins and intracellular tau tangles, and (N) neurodegeneration [8], [20].

Although the techniques currently used to diagnose AD have good predictive accuracy and are widely accepted by the medical community, they have some drawbacks that hinder their utility; neuroimaging is quite costly and spinal taps (used to measure cerebrospinal fluid - CSF - levels of tau and Aß) are extremely complex and invasive procedures [12], [14], [24], [46]. As such, there is a pressing need to develop less-expensive and less-invasive diagnostic methods for AD [7], [47], [48], preferably ones that could detect early-stage AD biomarkers in peripheral blood [12], [14], [46]. Blood biomarkers are not only easy to collect and analyse, but have the advantage of facilitating the monitoring of disease progression, which is crucial in AD where neuropathological changes often occur many years prior to symptom manifestation [14].

Biomarkers

Biomarkers are defined as any chemical indicators that can be used to assess the risk of a particular disease [14]. Despite the dire need for new early-stage AD biomarkers [7] and the vast amount of studies on the subject, the development of AD (and CNS disorders in general) biomarkers is lagging behind. This has been attributed to the complexity of the mechanisms involved, the neuroanatomy and brain function, the inaccessibility of brain tissue, and to various confounding factors (such as environment-gene interactions, heterogeneity of CNS disorders and stratification of the population sample) [6]. Furthermore, much of this effort has been dedicated to blood-based protein biomarkers, that a have a notably limited ability to cross the blood-brain barrier [47].

Recently, microRNAs (miRNAs) and, more specifically, circulating microRNAs (cimiRNAs) have been appointed as promising biomarkers for AD [6], [7], [12], [14], [23], [24], [46], [49], [50]. cimiRNAs can be found in a variety of fluids, including plasma, serum, urine and CSF [12] and their quantification may provide a method for early disease diagnosis [51]. In particular, miR-34a has shown great promise as a biomarker for AD [52].

1.2 - microRNAs

miRNAs are a class of endogenous small noncoding RNAs firstly reported in 1993 by Lee and colleagues [53]. miRNAs are usually around 18-24 nucleotides long and regulate mRNA translation [14], [25], [31], [49], [54], [55]. They work by binding with the Argonaute 2 (Ago2) protein in an RNA-induced silencing complex (RISC), which then binds to the target mRNA sequence (complementary to the miRNA) to silence its expression through translational inhibition or mRNA degradation [6]. Binding to the complementary sequences of mRNA occurs in the 3' untranslated regions (UTRs) of the target [27], [31], [55], [56] and is controlled by the seed region (situated between positions 2 and 8 of the sequence) [11]. Some studies even suggest that the interaction with mRNAs can go beyond the seed region and that miRNAs may also be able to home in on loci in the 5'-region or the protein-coding domains of their target mRNAs [23].

miRNAs are deeply involved in biological hallmarks, such as development, apoptosis, inflammation, proliferation, migration, invasion, metabolism, and differentiation [25], [50], [51], [57]. Moreover, miRNAs are thought to mediate paracrine, endocrine and juxtracrine signalling [24]. Recent research also found that certain miRNAs, such as miR-34a, can play a role in autocrine signalling [58]. Furthermore, miRNAs play a role in nervous system development and function, regulating processes such as neuronal patterning, synaptogenesis and neuronal plasticity [51]. In fact, dysregulation of miRNAs has been associated with neurodegeneration as well as the pathways known to be involved in neurodegeneration (e.g., mitochondrial dysfunction, inflammation, protein misfolding) [31], [59]. miRNAs are also thought to play a part in repressor element-1 silencing transcription factor (REST) expression in the brain, impairing its fundamental protective function against neurodegeneration. Finally, miRNAs are responsible for regulating up to hundreds of genes, lots of them associated with OS [31]. Owing to their prominent role in fine-tuning gene expression [55], over a thousand miRNAs have been associated with pathological conditions [6], reinforcing their role as physiological state predictors [46], [56].

With the development of nanobiotechnology and laboratory medicine, miRNAs have gained traction and have been appointed as promising biomarkers for a plethora of pathologies [53]. miRNAs possess several characteristics that make them well-suited for this task: they are stable, they can be quantified, they are resistant to RNAse digestion and to extreme conditions (e.g., extended storage, high temperature, extreme pH, multiple freeze-thaw cycles), and they can be secreted into the bodily fluids [7]. miRNAs can passively (energy-free) enter the circulation after changes in permeability or damage to the cell membrane (in case of apoptosis, metastasis, or inflammation). They can also be actively excreted by the cells as summarized on Figure 3 [6].

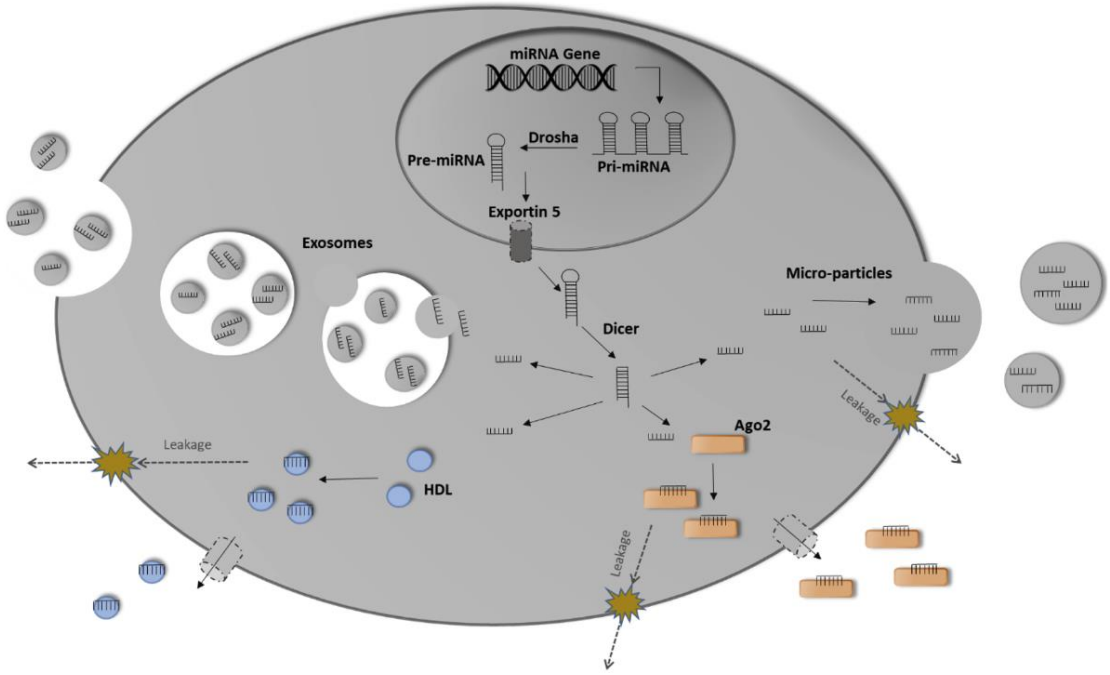

Figure 3 – Formation and excretion of mature miRNAs into the extracellular space. HDL: high-density lipoproteins; Ago2: Argonaute 2. Extracted from *van den Berg et al., 2020* [6].

Briefly, the RNA polymerase II transcribes miRNA genes into pri-miRNAs, in the nucleus. The resulting long pri-miRNAs are then processed by Drosha into shorter pre-miRNAs which are transported to the cytoplasm. Afterwards, Dicer cleaves the pre-miRNAs into mature miRNAs [6], [52] that are actively released into the extracellular space by vesicles, such as exosomes (inward budding), or micro-particles (outward budding). Alternatively, the miRNAs associate themselves with high-density lipoproteins (HDL) or Argonaute 2 (Ago2) to form complexes that are actively released into the circulation [6].

cimiRNAs can be found in a variety of fluids [12], usually in an vesicle-independent or free-floating form, bound to Ago2 [60]; however, the cells contained in whole blood samples can impair accurate cimiRNA detection. Likewise, the coagulation process variability in serum can impair this process. As such, plasma seems to be the best choice to analyse cimiRNA profiles [6], [61].

miR-34a

miR-34a is part of the miR-34 family [62], a family of tumour suppressive miRNAs firstly identified as an epigenetic component of the p53 network. Its activation promotes cell apoptosis and inhibits tumorigenesis [54]. In humans, miR-34a is encoded on chromosome 1 and, although ubiquitously expressed throughout the body, its concentration is particularly high in the brain [62].

miR-34a has long been associated with oncogenic pathways and malignancies [52], [62]; however, recent evidence suggests a link between miR-34a and neurophysiology/ neuropathology [56], [59]. In particular, miR-34a has been linked to the ability to regulate pre- and post-synaptic neuronal excitability, glycolysis, mitochondria oxidative phosphorylation, and resting state functional connectivity [26]. According to data extracted from the online database miRTarBase, miR-34a interacts with three target genes – BCL2 (Bcl2 apoptosis regulator), STX1A (syntaxin 1A) and SYT1 (synaptotagmin 1) – involved in a vast array of important cellular processes [20]. Bcl2 is anti-apoptotic protein that has neuroprotective effects against the amyloidogenic peptides [63] and its repression has been shown to lead to apoptosis and to an enhanced susceptibility to neurotoxic agents [59], [64]. STX1A interacts with several types of ion channel and neurotransmitter transporters, and is a crucial component of the complex that regulates neurotransmission at the synapses [65]. SYT1 participates in the release of neurotransmitters from presynaptic nerve terminals [66].

Recent cumulative evidence also suggests that miR-34a may play a part in AD pathophysiology [45], [52], [59]. Despite some discrepancies reported about the expression profiles of miRNAs in AD, miR-34a stands out as an example of increasing data reliability [23]. Firstly, this miRNA was found to be upregulated in the temporal cortex [32], frontal cortex and hippocampus of early AD subjects (Braak stages III-IV) [67] and positively correlated with the severity of AD pathology [7]. Secondly, the expression profile of miR-34a in the peripheral blood of AD patients was dysregulated and its expression profile was augmented in the CSF [31]. Thirdly, the overexpression of miR-34a in the brain of mice was associated with cognitive impairment, tau hyperphosphorylation and accumulation of intracellular Aß [52]. Moreover, this overexpression was linked to a decrease in Bcl2 levels in both mouse and cellular models [45], [59], [63]. Fourthly, SH-SY5Y cellular models showed that the downregulation of miR-34a decreases the protein levels of active caspase-3 (effector caspase that participates in late-stage apoptosis), which strengthens the link between miR-34a aberrant expression, apoptosis and neuroprotection [63]. Finally, overexpression of miR-34a was shown to reduce OS tolerance

by targeting the SIRT1/p66shc pathway [31]. SIRT1 – sirtuin (silent mating type information regulation 2 homolog) 1 – is a NAD-dependent histone deacetylase involved in various biological activities [54], including neuroprotective signalling. SIRT1 has been shown to reduce the formation of Aß. Conversely, Aß amyloidosis was shown to activate p53, activating miR-34a and, thus, suppressing SIRT1 [56]. p66shc expression is supressed by SIRT1 and has been shown to induce oxidative stress by producing a large amount of reactive oxygen species (ROS). This establishes the positive feedback loop between miR-34a, p53 and SIRT1 [6] which is depicted in Figure 4 [54]. OS also plays a role in this pathway, promoting the upregulation of miR-34a which further enhances the loop and weakens the OS defence pathways. It is worth noting that the weakening of OS defences has been proposed as one of the main factors for the development and progression of neurological diseases, such as AD [6].

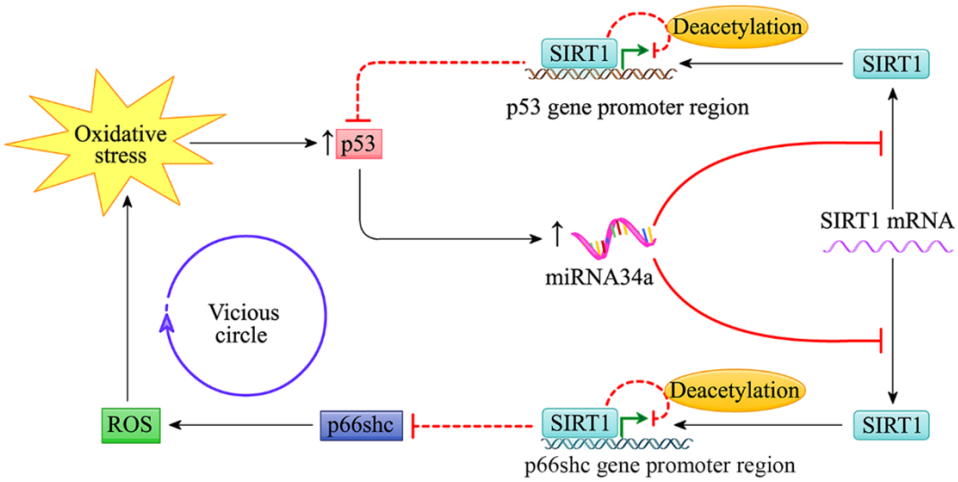

Figure 4- Schematic representation of the interaction between miR-34a, SIRT1 and p53. ROS: reactive oxygen species. Adapted from *Tong et al., 2019* [54].

In summary, miRNAs (including miR-34a) are promising biomarkers for many pathologies (including AD) which may provide a more reliable and less-invasive alternative for disease diagnosis. For miRNA detection in cell-free body fluids, biosensors are an enticing option since they are faster, simpler and require smaller sample volumes than conventional methods [51].

1.3 - Electrochemical biosensors

Currently, there is a pressing need in the field of clinical diagnosis for specific, selective, and sensitive tools for the detection and/or determination of various analytes. Different platforms have been developed for this purpose, including those based on the interactions between a biological sensing element (such as an antibody, nucleotide or enzyme) and the target analyte – biosensors [68]–[70].

Electrochemical sensors

Electrochemical sensors consist of three parts: counter electrode (CE), working electrode (WE) and reference electrode (RE) [69]–[73]. The WE is where the electrochemical reaction takes place; the RE, as the name implies, is a reference point for the potentials recorded on the other two electrodes; the CE is used to create a closed circuit of electrons in the sensor [72], [74]. The WE and CE should be made up of redox-inert materials whereas the RE should

be made up of a material with a stable and well-known potential, such as silver [74]. In commercially available sensors, the WE is generally circular and is surrounded by the RE and the CE [71]. To ensure a correct flow of electrons from the WE to the CE, the CE should have a larger surface area than the WE [74].

Electrochemical sensors have several advantages; they are portable, sensitive, low-cost, suitable for miniaturization, fast responding, adequate for small sample volumes, easy to use, suitable for a wide range of concentrations, and associated to low limits of detection (LODs) - achieving femto-picomolar LODs [49], [50], [71], [75]. Electrochemical biosensors, in specific, are also promising point-of care (POC) tools, as they allow fast results and direct sample reading, avoiding transportation of samples to the laboratory [49]. The low-cost aspect of electrochemical sensors becomes even more pronounced when using screen-printed electrodes (SPEs), particularly when using carbon-based SPEs (C-SPEs), which can be mass-produced in a fairly inexpensive manner [73], [76]. These are one of the most common types of sensors nowadays because they are not only inexpensive, but also have wide electrochemical windows and moderate catalytic activities for various types of redox probes [77].

Electrochemical analysis

Electrochemical analysis relies on the principle of detecting electrical changes in the transducer due to an interaction with the chemical analyte. These changes can occur either in current or voltage and can be detected by manners of potentiometric, amperometric, or impedimetric measurements [14], [69], [71]. Changes are often detected via a chemically active reporter, often a small redox molecule or an enzyme-substrate pair [49]. Redox probes should exhibit fast kinetics but should not interact with the surface of the electrode. Therefore, there is a tendency to use model probes for this purpose. The hexacyanoferrate (III)/(II) redox couple is one of the most commonly used model probes and often appears under the form of equimolar mixtures of hexacyanoferrate (II) and hexacyanoferrate (III) [78].

Voltammetry encompasses a large group of electrochemical techniques based on microelectrolysis [72]. They are commonly used for redox species characterization and analytical determination, but can also be used for other purposes, such as the study of adsorption phenomena or the thermodynamics/ kinetics of charge transfer [72], [74]. Voltammetry relies on the application of an electrical potential difference to cause non-spontaneous, interfacial charge transfer processes [72]. In other words, voltammetry studies the variation in the output current (I) of the system as a response to a variation in its input potential (E) [72], [74].

The most common, simplest and fastest form of voltammetry is cyclic voltammetry (CV) [70]. This technique is characterized by the ability to drive the system both in anodic and cathodic directions and by the potential ramp applied to the system. The typical potential ramp applied during CV is exemplified on Figure 5A [72]. The left side of the ramp represents the reduction of the chemically active species, whereas the right side represents its oxidation. This potential ramp produces a duck shaped *I vs. E* curve called a voltammogram, which is represented on Figure 5B. The two main features of a voltammogram are the anodic/ cathodic peak current (I_p) and peak potential (E_p) [72]. When the process is chemically and electrochemically reversible, the difference between the anodic peak potential ($E_{p,a}$) and the cathodic peak potential ($E_{p,c}$) has a characteristic value. In a single electron system, this difference, also referred to as the peak-to-peak separation (ΔE_p), corresponds to 57 mV (at 25 ºC) [74].

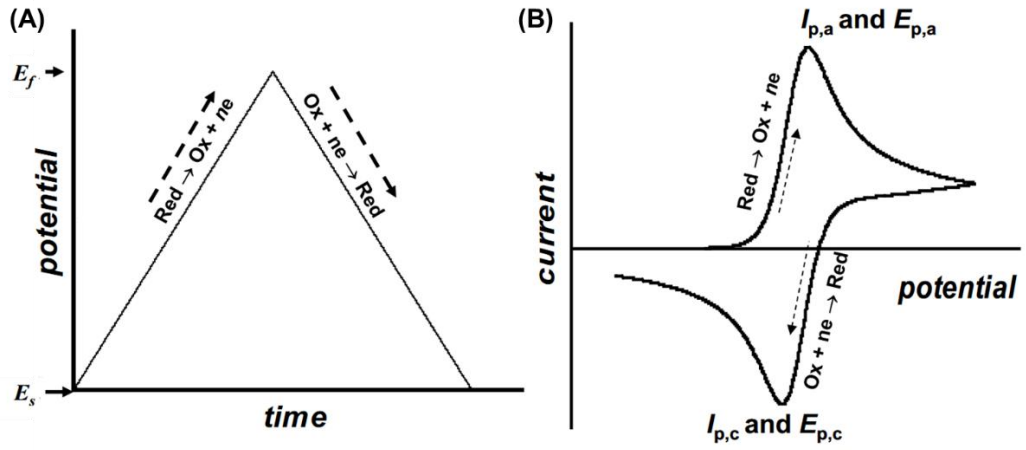

Figure 5 - Typical profiles of the potential ramp (A) and the voltammogram (B) of a CV assay. E_s: start potential; E_f: final potential; Red: reduced species; Ox: oxidized species. Adapted from *Mirceski et al., 2018* [72].

Another widely used form of voltammetry is square-wave voltammetry (SWV). The concept behind this technique is very similar to the previous one, except it uses a succession of square-wave pulses to create a stepwise potential ramp rather than a continuous potential ramp. This results in the staircase variation of potential depicted on Figure 6A.

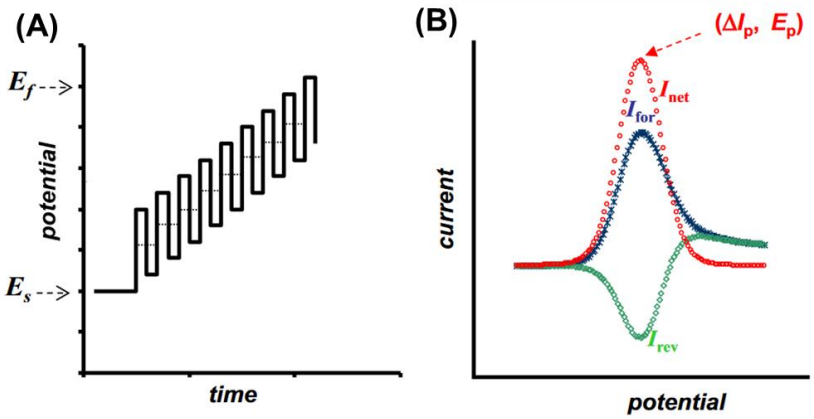

Figure 6 - Typical profiles of the potential ramp (A) and the voltammogram (B) of a SWV assay. E_s: start potential; E_f: final potential. Adapted from *Mirceski et al., 2018* [72].

A SWV potential cycle consists of two consecutive and oppositely directed pulses; the first is the forward pulse and the second is the reverse pulse. The typical voltammogram produced by SWV is represented on Figure 6B. The SWV voltammogram consists of three curves: the forward current (I_{for}) curve, the reverse current (I_{rev}) curve, and the net current (I_{net}) curve. The forward and reverse curves are experimentally measurable, while the net curve is calculated from the two previous curves. In fact, the net current corresponds to the subtraction of the reverse current to the forward current ($I_{net} = I_{for} - I_{rev}$). Although SWV voltammetry provides essentially the same information as CV, SWV has the higher sensitivity of the pulse voltametric techniques [72].

In addition to voltammetry, electrochemical impedance spectroscopy (EIS) is another powerful technique for electrochemical analysis. EIS is based on the idea that the processes associated with the electrolyte/interface and redox reactions can be represented as an

electrical circuit. A combination of resistors, capacitors, and/or inductors are connected to form an equivalent circuit that accurately calculates the mass-transfer, charge-transfer, and diffusion processes occurring at the surface of the electrode. Figure 7 shows one of the simplest examples of the translation of an electrochemical cell (the Randles simplified cell) into its equivalent circuit (the Randles simplified circuit) [70]. The Randles equivalent circuit is formed by two resistors and one capacitor. The two resistors represent the resistance to the movement of charge (typically electrons) across the interface – charge transfer resistance (R_{ct}) – and the inherent resistance of the electrolyte (R_s). The capacitor represents the charge separation that occurs at the interfacial region, known as the electrical double layer – double layer capacitance (C_{dl}) [70], [78]. In electrochemical sensors, all important interfacial phenomena are focused near the WE due to the high availability of electrolytes and the way the sensor is fabricated; thus, the modelling of equivalent circuit can be restricted to this region [78].

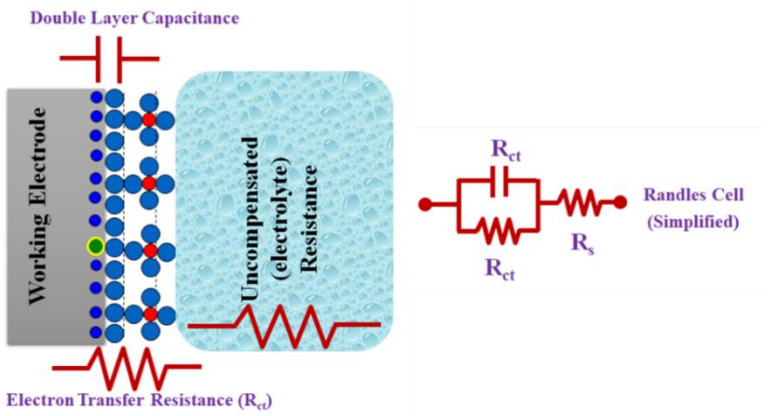

Figure 7 – Schematic representation of the Randles simplified cell and its corresponding Randles simplified circuit. Adapted from *Magar et al., 2021* [70].

EIS focuses on measuring the impedance of the equivalent circuit, i.e., its ability to resist the flow of electrical current. The impedance of the circuit is usually measured by applying a sinusoidal potential to the electrochemical system and observing its current response [78], [79]. Generally the potential wave applied is small (around 10 mV) to obtain a linear response and facilitate spectral analysis [78]. Knowing the input potential (E), and measuring the corresponding output current (I), it is possible to determine the impedance of the system (Z). Equation 1 shows how to calculate Z from E and I. Note that Z_0 represents the impedance magnitude and Φ represents the phase shift between E and I [70], [78], [79].

$$Z = E/I = Z_0 \exp(i\Phi) = Z_0 (\cos\Phi + i \sin\Phi) = Z' + i Z'' \quad \textbf{(Equation 1)}$$

Looking at Equation 1 one can see that the impedance can be divided into a real part (Z_{real} or Z') and an imaginary part ($Z_{imaginary}$ or Z''). Graphically, the impedance can be represented by a Nyquist Plot, where the Z' is plotted on the X-axis and the Z'' is plotted on the Y-axis [70], [78], [79]. The shape of the Nyquist Plot is variable and dependent on the characteristics of the electrode matrix as well as the electrochemical processes in place, but it is always representative of the various components of the equivalent circuit. Figure 8 shows a variety of the shapes that Nyquist Plots can take as well as the corresponding equivalent circuits [70].

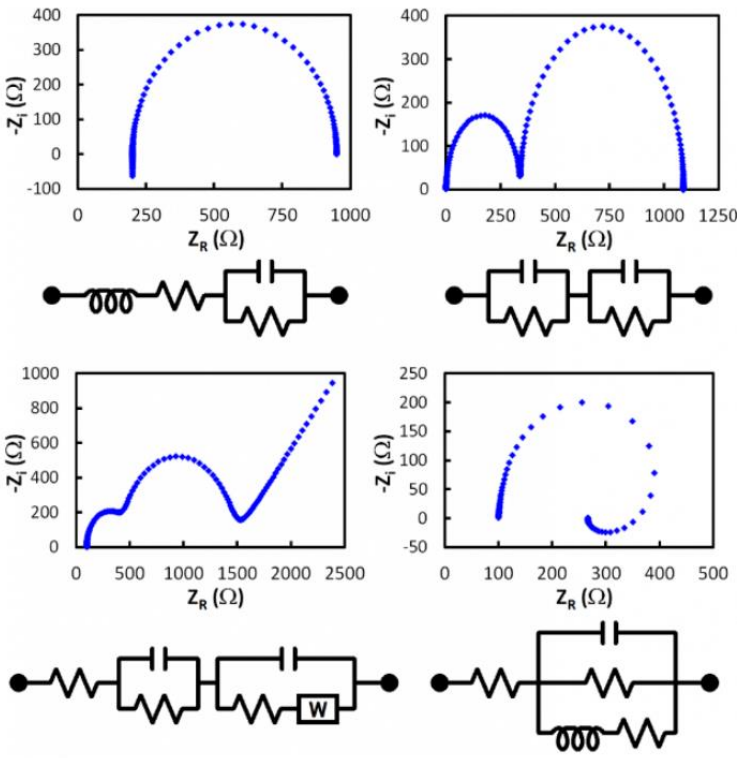

Figure 8 – Examples of a variety of electrochemical circuits and their corresponding Nyquist plots. Extracted from *Magar et al., 2021* [70].

In a simplified Randles equivalent circuit, the resistance of the electrolyte (R_s or R_Ω), the double layer capacitance at the surface of the electrode (C_{dl}), and the charge transfer resistance (R_{ct}) can be extracted from the Nyquist Plot as exemplified on Figure 9 [70], [78].

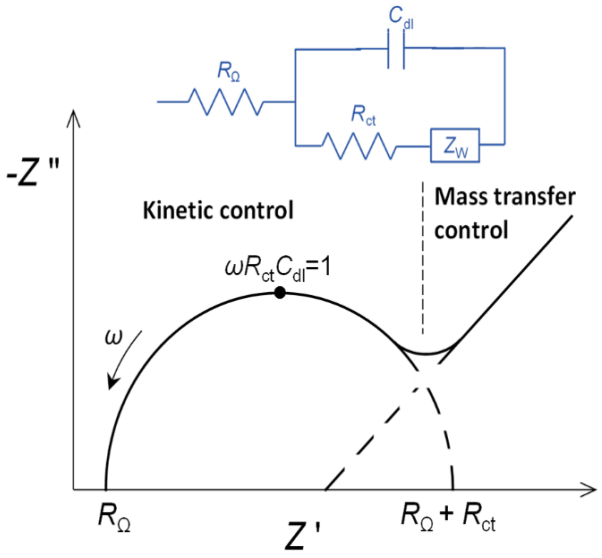

Figure 9 – Relationship between the resistance of the electrolyte (R_Ω), the double layer capacitance at the surface of the electrode (C_{dl}), the charge transfer resistance (R_{ct}) and the Nyquist Plot of the circuit, in a simplified Randles circuit. Adapted from *Brett, 2022* [78].

Briefly, R_{ct} corresponds to the diameter of the semi-circular region, R_{Ω} to the lowest X-axis intercept and C_{dl} can be calculated using Equation 2, where ω represents the radial frequency of the excitation signal [78].

$$\omega R_{ct} C_{dl} = 1 \quad \textbf{(Equation 2)}$$

EIS is one of the best electrochemical analysis techniques to be use with biosensors as it can detect small changes in reactive surfaces (such as those caused by the hybridization of the target with the probe) and perform well in complex solutions, such as serum [50], [57]. Moreover, EIS allows the follow-up of each modification/ immobilization step, making it a powerful detection technique for the monitoring of biosensors [80].

Electrochemical biosensors

Electrochemical biosensors are label-free sensors [14], which means they can directly measure the interactions between the probe and the target analyte, eliminating the need for labels and reacting procedures [81]. This greatly reduces the cost and detection times of the sensor, while increasing sensitivity and specificity [14], [81]. Although biosensors have been mainly used to detect large molecules, they can also be applied to small molecular weight chemicals. For example, *Lin et al.* developed an impedimetric label-free sensor for the detection of salbutamol based on C-SPEs modified with Au NPs. The Au NPs were used to add roughness to the surface of the WE, to compensate for the effect of the smaller steric changes associated with low molecular weight chemicals [81].

Nanogold-based sensors

Nanotechnology has been shaping medicine since the 20th century, with the discovery of immunogold labelling in the 1970s [82]. In the last decade, nanotechnology has experienced an exponential growth. Nanoparticles (NPs) – typically, particles with a diameter smaller than 100 nm [83], [84] – have found application in various fields [85], from materials science [86] to medical practice [87]. These advances in nanomaterials and analytical technologies have also opened new opportunities in the field of biosensor fabrication [69], [88], [89].

Nanomaterials possess unique physicochemical properties (such as high absorption capacity, good surface-to-volume ratio, and reactivity) that make them attractive for biosensor construction. Nanoscale patterning of electrodes has been shown to improve biosensor performance, by either amplifying the signal (through catalytic activity and conductivity), facilitating interfacial recognition of the target (by accelerating molecular diffusion or reducing steric hindrance) or enabling precise immobilization of functional moieties [75], [76].

Nanomaterials can appear in many shapes (such as particles, wires or layers) [83], [90] and can be made up of several types of materials (including polymers, metals, metal-oxides and carbon) [84]. Noble metal nanoparticles (e.g., gold (Au), silver (Ag), palladium (Pd) and platinum (Pt)) have been employed in biosensors mainly due their unique size- and shape-dependent physicochemical and electrochemical properties [88] which greatly improve the sensitivity and sensibility of the sensors [75]. Gold nanoparticles (Au NPs) are highly stable and easy to fabricate, have a high surface-to-volume ratio, make complete recoveries in biochemical reactions, have a great catalytic ability, and can withstand a wide range of electrochemical potentials [76], [81], [88]–[93]. Electron transfer is also greatly improved by the use of Au NPs in the electrodes [89]. Furthermore, Au NPs react well with organosulfur

compounds through Au-S covalent bonds and allow the formation of stable self-assembled monolayers (SAMs) [93]. Altogether, the inherent properties of Au NPs favour miniaturization of the sensing platforms and further enhance their applicability in biosensor construction [88], [89].

The fabrication of gold-based biosensors entails the preparation of a conducting platform made up of Au NPs. As with all biomaterials, this can be achieved by two approaches: bottom-up or top-down. The bottom-up approach relies on the connection of smaller particles (e.g., atoms) to form NPs, whereas the top-down approach implies reduction of the bulk material to smaller-sized NPs. One example of the bottom-up approach is chemical reduction, such as the one that occurs during electrodeposition [94]. Lately, electrodeposition has been gaining momentum in this field on accounts of its green and controllable procedure [92], which is based on the reduction of Au^{3+} ions in aqueous solution to elemental gold (Au^0). The chemical reaction behind electrodeposition is explained on Equation 3 [76].

$$[AuCl_4]^- + 3\ e^- \rightarrow Au^0 + 4\ Cl^- \qquad \textbf{(Equation 3)}$$

The formation of Au NPs through this technique involves two mechanisms (nucleation and growth) and can be divided into three stages: (i) formation of nuclei, (ii) aggregation of small particles to the nuclei, and (iii) growth of the nuclei into crystals. The reaction conditions (e.g., electrodeposition potential, electrochemical technique, and electrodeposition time) are paramount to the processes of nucleation and growth and, therefore, have great influence on the morphology of the formed Au NPs [76], [90]. A recent study by *Hou et al.* on the electrodeposition of Au NPs from acidic medium on glassy carbon electrodes (GCEs) showed that nucleation is controlled by the deposition potential whereas particle growth is controlled by the deposition time [92].

Electrodeposition can be achieved through CV or chronoamperometry (CA) [91]. For example, *Zhao et al.* produced a gold-based biosensor for the detection of bisphenol A via electrodeposition of Au NPs through CV. Briefly, pre-treated GCEs were immersed in a 10 mM $HAuCl_4$ solution (prepared in 0.5 M H_2SO_4) and subjected to 15 CV cycles in the potential range of −0.2 V to +0.6 V, at 50 mV/s. This produced a film of uniform Au NPs on the surface of the electrodes which favoured their functionalization, due to increased surface area and pathways for ion transport. Moreover, the gold film improved the conductivity of the sensor and enhanced its response current [95]. On the other hand, *Brazaca et al.* produced an electrochemical immunosensor for the detection of the S proteins from SARS-CoV and SARS-CoV-2 based on chronoamperometrically deposited Au NPs. The particles were deposited by dipping the electrodes in 20 mL of a 5 mM $HAuCl_4$ solution (prepared in 0.5 M H_2SO_4), under vigorous stirring, and applying a constant potential of − 4.0 V for 9 s, 30 s or 90 s. This resulted in the formation of a homogeneous thin film of Au NPs on the surface of the electrode, which enhanced its sensitivity [73]. Likewise, *Hou et al.* showed on the aforementioned study that the chronoamperometric electrodeposition of Au NPs from acidic medium onto GCEs was possible and augmented the surface area of the electrodes. Furthermore, they showed that this technique produced a monolayer of gold on the surface of the electrode which significantly improved its electrocatalytic activity [92].

miRNA-based sensors

Over the last twenty years, the incorporation of biopolymers, proteins/enzymes, or nucleic acids into the design of biosensors has attracted considerable attention as it can improve their sensitivity and biocompatibility, as well as their response and recovery time [48], [88]. Conversely, the inclusion of oligonucleotides in electrochemical biosensors facilitates the application of miRNAs as clinical biomarkers, since conventional miRNA detection techniques (e.g., Northern blotting, isothermal exponential amplification-based methods and rolling cycle amplification-based methods) are expensive, complicated and time consuming [50], [57]. Therefore, miRNA-based biosensors have gained traction and their use is increasing every day [80].

Most miRNA-based biosensors are affinity biosensors, which means they use a biological molecular probe that is immobilized on the transducer to detect probe-target interactions [69]. Electrochemical miRNA biosensors typically use a mostly linear oligonucleotide strand as the recognition element [49], and rely on the hybridization of the probe sequence with the complementary target sequence to cause a measurable change in the electrical properties of the electrode or its interface [49], [69].

To date, a few electrochemical miRNA-based biosensors have already been proposed for disease diagnosis. For example, *Carneiro et al*. developed a homemade 3-carbon electrode system for detection of miR-107, a potential biomarker for AD [71]. *Rafiee-Pour et al*. produced GCEs modified with multi-walled carbon nanotubes for the detection of miR-21, a cancer biomarker [96]. *Vanova et al*. also developed GCEs for the detection of this same miRNA, except this time modified with electrochemical reduced graphene oxide [97]. *Cardoso et al*. developed a modified Au-SPE for the detection of miR-155, a breast cancer biomarker [49]. Despite the excellent analytical performance reached by this construct (which was able to detect attomolar concentrations of miRNA-155 in real human serum samples [49]), using gold as a substrate can become rather expensive. To circumvent this problem, gold use may be restricted to a portion of the substrate. One way to do so is by modifying the surface of the electrodes with gold nanostructures [51], as described in the previous section. This technique has already been successfully employed, for example, by *Serrano et al*. or *Bharti et al*. *Serrano et al*. developed C-SPEs modified with electrodeposited Au NPs for the detection of miR-21-5p [51]. *Bharti et al*. constructed a fluorine-doped tin oxide platform modified with a gold platinum bimetallic nanoparticles/3-aminopropyltriethoxy silane nanocomposite for the detection of miR-21 [98]. Both maintained a good analytical performance (showing a linear response within the femtomolar range) [51], [98] whilst reducing the costs related to the gold utilized for biosensor construction.

Focusing on miR-34a, the biomarker of interest in this project, some biosensing platforms have already been designed for the detection of this oligonucleotide. Despite using different types of electrodes and surface modifications, all these platforms detected miR-34a through the change of electrochemical properties that occurs when the miR-34a strands in solution hybridize with the anti-miR-34a strands immobilized on the surface of the electrodes. For example, *Congur et al*. proposed graphene oxide modified pencil graphite electrodes (PGEs) for the detection of miR-34a, which showed a linear response within 0 to 10 µg/mL [57]. *Kesici et al*. also proposed PGEs for this purpose, however, this time modified with 1-butyl-3-methylimidazolium hexafluorophosphate; their platform demonstrated a similar range of linearity, between 2 and 10 µg/mL [50]. Similarly, *Mandli and Amine* developed polypyrrole-modified PGEs for the detection of miR-34a; however, the range of linearity was much broader,

going from 5 to 80 µg/mL [99]. *Congur and Erdem* opted for a completely different approach and designed a poly(amidoamine) dendrimer-modified graphite SPE for the detection of miR-34a, which displayed a linearity range of 0 and 7.5 µg/mL [80]. Overall, all the examples reported were selective for miR-34a and showed a linear response within tenths of µg/mL of miR-34a.

Driving inspiration from the previously discussed electrochemical biosensors and considering the high socioeconomic impact of AD, this work focuses on the development of a new miRNA-based biosensor for the detection of AD. The idea is to modify commercially available C-SPEs firstly with a nanostructured gold layer and secondly with an anti-miR-34a oligonucleotide probe, in order to detect circulating miR-34a. This strategy combines the cost-effectiveness of C-SPEs with the unique electrochemical properties of gold nanostructures and the specificity of miRNAs and aims to provide a new POC platform for AD diagnosis. Hopefully, this system will one day reach the clinical setting and bring patients and physicians a simpler, less-invasive alternative to the existing AD detection tools. Although this is non-curative platform, it may help diagnose patients at an earlier stage of the disease, broadening their treatment options and improving their outcomes.

Chapter 2

Experimental

2.1 - Reagents and solutions

The chemicals used in the experiments were all analytical grade. Solutions were prepared with ultrapure water (obtained from a Milli-Q water purification system) or ultrapure water treated with DEPC 0.1% to protect the miRNA from RNAse degradation.

Potassium hexacyanoferrate II-3-hydrate ($K_4[Fe(CN)_6]$), magnesium chloride 6-hydrate ($MgCl_2.6\ H_2O$), and potassium hexacyanoferrate III ($K_3[Fe(CN)_6]$) were obtained from Riedel de Haën; disodium hydrogen phosphate ($Na_2HPO_4{\cdot}2H_2O$) from Carlo Erba; sodium dihydrogen phosphate dihydrate ($NaH_2PO_4{\cdot}2H_2O$) from Scharlau; L-Asparagine (Asn, $C_4H_8N_2O_3$), diethylpyrocarbonate (DEPC) 99% ($C_6H_{10}O_5$), sulfuric acid 95-97% (H_2SO_4), 3-mercaptopropionic acid (3-MPA, $C_3H_6O_2S$), 1-ethyl-3-(3-dimethylaminopropyl)carbodiimide (EDAC), 4-(2-hydroxyethyl)-1-piperazineethanesulfonic acid (HEPES, $C_8H_{18}N_2O_4S$), and ammonium chloride (NH_4Cl) from Merk; N-hydroxysuccinimide (NHS) and creatinine ($C_3H_3NO_2$) from Fluka; sodium chloride (NaCl) from Normapur; hydrogen tetrachloroaurate (III) hydrate ($HAuCl_4{\cdot}xH_2O$) from Alfa Aesar.

Oligonucleotide sequences (anti-miR-34a, miR-34a, and miR-107) were obtained from MeTabion. Both the anti-miR-34a and the miR-34a used for calibration are mimetic models, of DNA nature. The anti-miR-34a has an amine 5′-end followed by poly-A spacers and its complete sequence is 5′-C6 NH_2-AAA AAA ACA ACC AGC TAA GAC ACT GCC A-3′. The miR-34a complete sequence is 5’-TGG CAG TGT CTT AGC TGG TTG T-3’. Finally, the miR-107 is of RNA nature and its complete sequence is 5′-AGC AGC AUU GUA CAG GGC UAU CA-3′.

Stock solutions of anti-miR-34a (300 nM) were prepared in Phosphate Buffer (10 mM Na_2HPO_4: 10 mM NaH_2PO_4, pH=7.4), whereas stock solutions of the miR-34a (300 nM) were prepared in ultrapure, DEPC-treated water. Both solutions were kept frozen at -20 °C. Subsequent dilutions of the miR-34a stock solution were prepared in Hybridization Buffer – Phosphate buffer with 50 mM $MgCl_2$ and 150 mM NaCl, at pH=7.4 or Phosphate buffer with 5 mM $MgCl_2$ and 150 mM NaCl, at pH=8.

DMEM (1x) + GlutaMAX™-I (Dulbecco’s Modified Eagle Medium supplemented with pyruvate and 4.5 g/L D-glucose), low-glucose DMEM (1x) + GlutaMAX™-I (Dulbecco’s Modified Eagle Medium supplemented with pyruvate and 1 g/L D-glucose), and foetal bovine serum (FBS) were

purchased from Gibco; gentamicin sulphate 50 mg/mL from Biowest; 4′,6-diamidino-2-phenylindole (DAPI), Flash Phalloidin™ Red 594, mouse anti-B-tubulin III antibody from BioLegend; IgG donkey anti-mouse antibody marked with Alexa Fluor 488 from Invitrogen™; ibidi Mounting Medium form ibidi GmbH; bovine serum albumin (BSA) from NZYTech; retinoic acid (RA), 6-hydroxydopamine (6-OHDA), Triton X-100, and paraformaldehyde (PFA) from Merck; trypsin-EDTA (0.25%) from Thermofisher scientific. Phosphate-buffered saline (PBS) was prepared in-house according to the laboratory's guidelines.

2.2 - Apparatus

The electrochemical data was obtained using the PGSTAT302N, a potentiostat/galvanostat equipment from Metrohm Autolab, controlled by Nova 2.1 software. Data extracted from the Nova 2.1 software was analysed using Origin. The C-SPEs were connected to the potentiostat via a box connector from BioTid Electronical.

The cell cultures were periodically visualized using an Olympus CKX41bright-field inverted microscope and a 10x objective.

The immunocytochemistry preparations were visualized using an Axiovert 200M inverted fluorescence microscope, from Zeiss and the images were acquired using a 40x oil objective and a black and white camera. Images were further analysed using ImageJ.

2.3 - Electrochemical assays

The electrochemical properties of the sensors were determined using an equimolar solution of $[Fe(CN)_6]^{3-/4-}$ (5 mM of $K_4[Fe(CN)_6]$: 5 mM of $K_3[Fe(CN)_6]$ in Phosphate Buffer, at pH=7.4).

CV assays were performed via 3 consecutive CVs, for signal stabilization, ranging from −0.4 to +0.7 V, with a scan rate of 50 mV/s. SWV assays were acquired in a −0.4 to +0.7 V range, using a frequency of 5 Hz and a step height (amplitude) of 20 mV. EIS was performed in an open circuit potential, with a sinusoidal potential perturbation of 0.01 V amplitude and 45 frequencies, over a 0.1 to 100,000 Hz frequency range.

2.4 - Modification of the commercial C-SPEs

Commercially available C-SPEs with a Ag reference electrode were modified either with gold nanoparticles (Au NPs) or a nanoporous gold (NP-Au) mesh, according to *Zhao et al.* [95] or *Moreira et al.* [100], respectively. In both cases, the electrodes were firstly subjected to 30 consecutive CVs (ranging from -0.2 to +1.0 V, using a scan rate of 100 mV/s) in 70 µL of 0.5 M H_2SO_4, to remove impurities and activate the surface. Then, 70 µL of a 10 mM solution of $HAuCl_4$ (in 0.5 M H_2SO_4) were added to the electrodes and the Au NPs were electrodeposited by 15 consecutive CVs (ranging from +0.6 to -0.2 V, using a scan rate of 50 mV/s). Alternatively, 70 µL of a 0.1 M solution of $HAuCl_4$ (in 1 M NH_4Cl) were added to the electrodes and the NP-Au mesh was electrodeposited by CA, by applying a potential of -0.7 V for 10 s, followed by a potential of -1.5 V for 10 s.

In each case, and anticipating the intended application of the sensor, the WE was further modified with 20 µL of 10 mM 3-MPA for 2 h (shielded from light to prevent photodegradation of the 3-MPA). The carboxylic groups in the 3-MPA were then activated by an EDAC/NHS

reaction: 10 µL of 12.5 mM NHS (in 10 mM HEPES buffer) were incubated in the WE for 5 min; then, 10 µL of 10 mM EDAC (in 10 mM HEPES buffer) were mixed into the NHS solution and left to incubate for an additional 25 min. Finally, the WE was functionalized for 1 h with 5 µL of a 10 µM anti-microRNA-34a solution and the non-specific binding sites were blocked with 5 µL of a 50 mM L-asparagine (Asn) solution for 1 h. Before being added to the WE, the anti-miR-34a solution was heated for 5 min at 90 °C to linearize the DNA strands and promote subsequent interactions with the complementary miR-34a strands. A schematic representation of the process of modification of the C-SPE is represented in Figure 10.

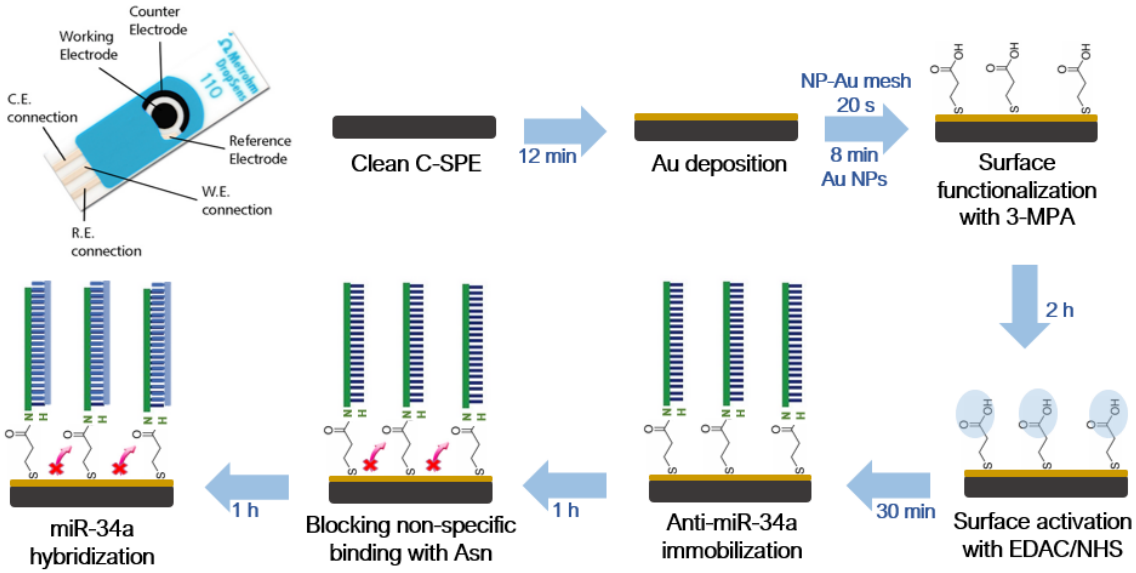

Figure 10 – Schematic representation of the biosensor's construction process. Image of the sensor obtained from the Metrohm DropSens' website [101].

It is worth noting that the construction process was performed at RT and that routine electrochemical assays were performed after each construction step (except EDAC/NHS activation) to ensure the correct assembly of the biosensor.

2.5 - Calibration of the sensor

Calibration of the sensor was performed in three different solvents: Hybridization Buffer, FBS, and cell culture medium. The FBS and cell culture medium were firstly diluted in Hybridization Buffer (1:100) and then filtered using a 100 kDa Amicon Ultra-2 Centrifugal Filter Unit from Millipore (2 mL of sample, filtered at 8500 g for 5 min). Dilutions were performed to ensure pH=7.4, whereas filtration was performed to minimize the interference of high molecular weight substances with the sensor.

Prior to calibration, the sensors were stabilized in solvent. For this purpose, 5 µL of solvent were incubated on the WE for 30 min. The sensors were then evaluated by electrochemical assays and the procedure was repeated until the EIS curves of the last two measurements overlapped. Subsequently, 5 µL of miR-34a solutions of rising concentrations (0.1 nM, 1 nM, 10 nM, 100 nM, and 1 µM) in solvent were incubated on the WE for 30 min. The R_{ct}, as well as the peak height of the SWV curves, were extracted using the Nova 2.1 software. Finally, calibration curves were obtained by plotting the logarithm of the miR-34a concentration against the normalized value of R_{ct} or against the maximum peak height (I_{max}).

2.6 - Specificity/selectivity tests

To assess the specificity/selectivity of the sensor, its response was evaluated in the presence of potentially interfering substances. Two potential interferents were tested: creatinine and microRNA-107. Both substances can be found in human plasma (one of the fluids chosen for future clinical application). Additionally, miR-107 has a similar nature to miR-34a, which increases the stringency of the test. The concentration of the interferents was set according to their physiological values and then diluted 100-fold to match the dilution performed for FBS. Even in clinical settings, dilution will likely be necessary to adjust the pH of the patient samples.

To perform these tests, the sensors were firstly stabilized in Hybridization Buffer. Then, 5 µL of the test solution were incubated on the WE for 30 min. The solutions were prepared in Hybridization Buffer and made up of 0.1 nM of miR-34a (i) by itself, (ii) with 10 fM of miR-107 or (iii) with 900 nM of creatinine. Afterwards, the EIS was measured, and the R_{ct} was extracted using the Nova 2.1 software. Finally, the variations in R_{ct} resulting from the incubation of the test solutions were compared against each other to determine whether the sensor performs similarly in the presence of potential interferents or not.

2.7 - *In vitro* proof of concept

Cell culture

SH-SY5Y cells were cultured in DMEM (1x) + GlutaMAX™-I supplemented with 15% FBS and 0.1% gentamicin sulphate 50 mg/mL. This medium will be further referred to as Non-differentiation Medium. The culture flasks were incubated in a humidified environment at 37 °C and 5% CO_2. The medium was changed regularly, and the cells were split with trypsin-EDTA at about 80% confluence.

Neuronal differentiation and collection of cellular media for analysis

Neuronal differentiation was performed using a protocol adapted from *Simões et al., 2021* [41]. Firstly, the cells were plated in a 96-well plate at a density of 20,000 cells/well (for differentiation) or 15,000 cells/well (to serve as non-differentiated control – Non-DIFF) and cultivated in Non-differentiation Medium (150 µL per well). 24 h after plating the medium was refreshed and, in the case of the cells meant to be differentiated, replaced with low-glucose DMEM supplemented with 1% FBS, 0.1% gentamicin sulphate 50 mg/mL and 10 µM RA – Differentiation Medium. RA was obtained from a stock concentration of 20 mM RA dissolved in dimethyl sulfoxide. 4 days after plating, the medium was refreshed or replaced with 100 µL of Differentiation Medium supplemented with 50 µM or 100 µM of 6-OHDA – DIFF_50 and DIFF_100. 6-OHDA is an oxidative metabolite of dopamine and a neurotoxin used to induce cytotoxicity in various cell types [42]. In this case, it was used to try to boost the expression and secretion of miR-34a into the cellular medium, as described by *Ba et al*. [44]. 5 days after plating (with 1 day under 6-OHDA stimulation), 50 µL of media were collected from each well, and the cells were prepared for immunocytochemistry.

The observe the morphology of cells and to ensure the cells remained healthy throughout the procedure, the cells were periodically inspected through bright-field microscopy.

Immunocytochemistry

To understand the effects of differentiation and exposure to the neurotoxicant stimulus (6-OHDA), the cells were subjected to immunocytochemical assays. After neuronal differentiation and media collection, the cells were fixed. For that, 50 µL of 8% PFA (in PBS) were added to the remaining 50 µL of culture media and incubated for 10 min, at room temperature (RT). Afterwards, the cells were washed once for 10 min with PBS and stored overnight in PBS, at 4°C, until analysis. The following day, the cells were washed with PBS for 10 min and permeabilized with 0.1% Triton X-100 for 5 min, at RT. Then, the cells were washed twice with PBS (10 min per wash) and unspecific binding sites were blocked by incubating the cells with BSA prepared in PBS – Blocking Solution – for 1 h, at RT. Afterwards, to stain ß-tubulin III, a microtubule element almost exclusively found in neurons, the Blocking Solution was replaced with the primary antibody solution (1:500 mouse anti-ß-tubulin III antibody in Blocking Solution) and incubated for 1 h, at RT. The cells were washed twice with PBS (10 min per wash) and the secondary antibody solution (1:1000 IgG Alexa 488 donkey anti-mouse antibody in Blocking Solution) was incubated for 1 h, at RT. From this incubation procedure onwards, the plate was protected from light to prevent fluorescence loss. To visualize the nuclei of the cells, the washing process was repeated, and the cells were incubated with a DAPI solution (1:10,000 in Blocking Solution) for 10 min, at RT. Then, the washing process was repeated, and the cells were incubated with a Flash Phalloidin™ Red 594 solution (1:40 in PBS), for 20 min, at RT. DAPI is a nuclear stain whereas phalloidin is a biomarker for F-actin (one of the major components of the cytoskeleton). Finally, after staining, the cells were washed again, and two drops of ibidi Mounting Medium were added to each well. The prepped plates were stored in PBS in the dark at 4°C until analysis.

Testing the sensor in cellular media extracts

To further validate the applicability of the biosensor herein described, the sensor was used to analyse the cellular media extracts previously obtained. Firstly, the sensors were stabilized in plain Differentiation Medium diluted in Hybridization Buffer (1:100) and then filtered using a 100 kDa Amicon Ultra-2 Centrifugal Filter Unit from Millipore (2 mL of sample, filtered at 8500 g for 5 min). This media had been previously incubated in one well of a 96-well plate alongside the cultured cells. Afterwards, each sensor received a media sample of one of the conditions tested – DIFF_0, DIFF_50 or DIFF_100. The samples were diluted in Hybridization Buffer (1:100) and then filtered using a 100 kDa Amicon Ultra-2 Centrifugal Filter Unit from Millipore (2 mL of sample, filtered at 8500 g for 5 min).

Lastly, the shift in R_{ct} caused by the presence of miR-34a in the samples was checked against the calibration curve previously obtained to gauge the concentration of miR-34a in each sample.

Chapter 3

Results and discussion

Before getting into this section, it is worth noting that the design process herein presented is only the final product of a long and iterative process. Many failed attempts were necessary before obtaining a sensor that was able to detect miR-34a. The designs of those failed attempts are summarized in the Annex. However, the author decided to omit the results obtained for those designs in this work as they would lead to an unnecessarily long and tedious read.

This section provides a rundown and a critical analysis of the results obtained for the assays on the Experimental section. Firstly, it is demonstrated that the design process is successful both for the Au NPs and the NP-Au mesh modified sensors. Afterwards, the choice of hybridization buffer and gold deposition technique is explained. Then, it is shown that the biosensor performs well under more stringent conditions, i.e., under calibration in FBS, cell culture medium or in the presence of possible interferents. Finally, the biosensor is shown to have a promising performance in an *in vitro* proof of concept.

3.1 - Modification of the commercial C-SPEs

To recapitulate the construction process of the biosensor, commercially available C-SPEs were firstly subjected to a pre-treatment in H_2SO_4 to remove impurities and activate the surface, i.e., to make it more reactive to better accommodate the gold layer deposition. Then, Au NPs were electrodeposited by CV [95] or a NP-Au mesh was electrodeposited by CA [100]. In every case, the WE was further modified with 3-MPA. As shown in Figure 11, MPA is a bifunctional molecule containing a thiol group in one end and a carboxylic group on the other end.

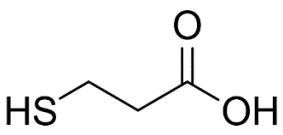

Figure 11 – Chemical structure of 3-mercaptopropionic acid [102].

The thiol group allows the 3-MPA to bind to the surface through a gold-sulphur interaction (like the one on SAMs) whereas the carboxylic group enables a carbodiimide reaction between the 3-MPA and the amine-terminated probe. To promote this reaction, the carboxylic groups in the 3-MPA were firstly activated by an EDAC/NHS reaction. EDAC reacts with the carboxylic groups of the 3-MPA to form an active O-acylisourea intermediate. The active O-acylisourea intermediate then reacts with the NHS to form an NHS ester, which is more stable than the O-acylisourea, and can still be easily displaced by the amine groups [103]. This facilitates the nucleophilic attack from the primary amine in the probe and promotes binding of the probe to the 3-MPA. Before functionalizing the WE with an anti-miR-34a (probe) solution, this solution was pre-heated to linearize the DNA strands and favour later interactions with the complementary miR-34a strands (target). Finally, unspecific binding sites were blocked with Asn.

The first two steps of the construction process were followed using all three electrochemical analysis techniques selected (CV, SWV, and EIS). Figure 12 depicts a representative example of the results obtained for the electrodeposition of Au NPs by CV.

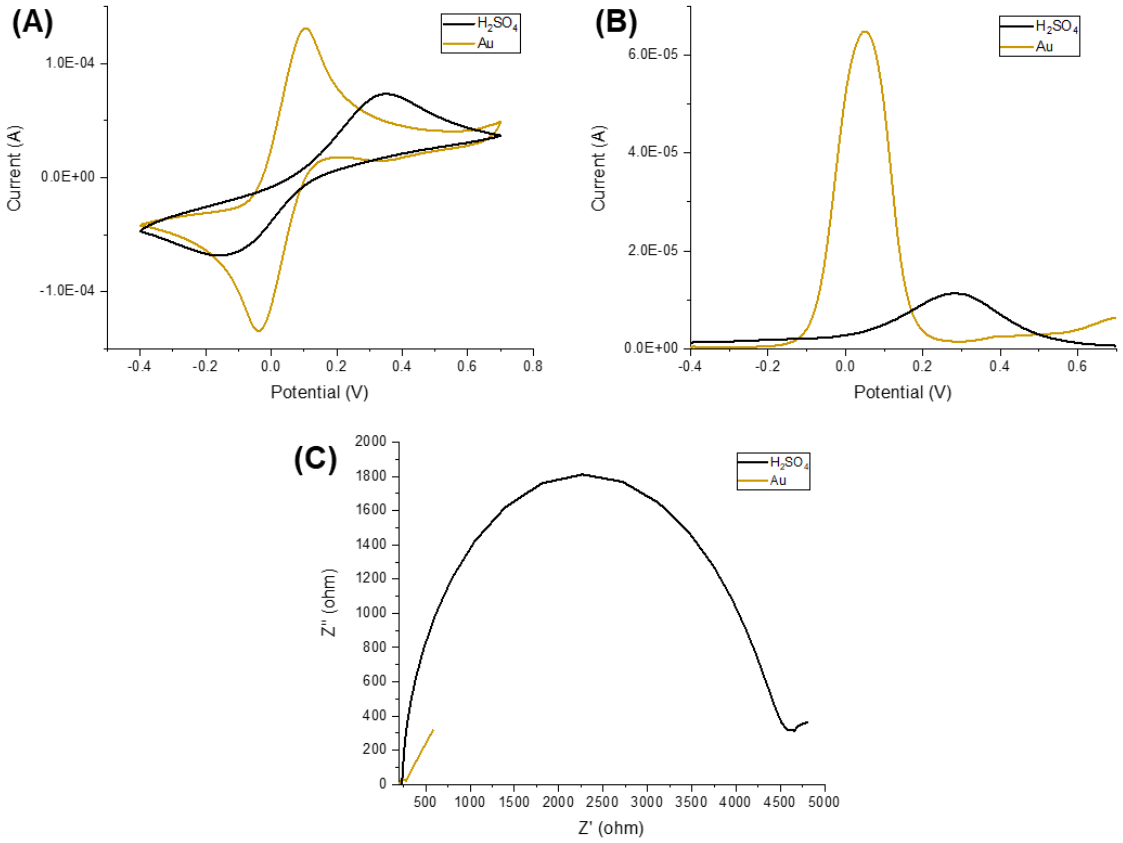

Figure 12 - Representative examples of the CV (A), SWV (B) and EIS (C) curves obtained for the electrodeposition of Au NPs by CV.

Figure 12A shows a smaller peak-to-peak separation, higher currents, and a "curvier" profile of the CV curve after gold deposition when compared to the CV curve after H_2SO_4 pre-treatment. Figure 12B also shows higher currents along with a lower peak potential of the SWV curve after gold deposition when compared to the SWV curve after H_2SO_4 pre-treatment. Finally, Figure 12C shows a decrease in the impedance and R_{ct} when shifting from the EIS curve

after H_2SO_4 pre-treatment to the EIS curve after Au NPs deposition, indicating that the Au NPs were successfully deposited.

Figure 13 depicts a parallel of these results, this time obtained for the electrodeposition of a NP-Au mesh by CA. Comparing Figure 13 with Figure 12, it is clear that the results obtained for the electrodeposition of the Au NPs are extremely similar to the ones obtained for the electrodeposition of the NP-Au mesh. The three analysis techniques show an increase in the conductivity (or a decrease in the impedance) of the surface after the deposition of the NP-Au mesh, indicating that this process was successful. Overall, at this stage, the two gold deposition techniques are equivalent.

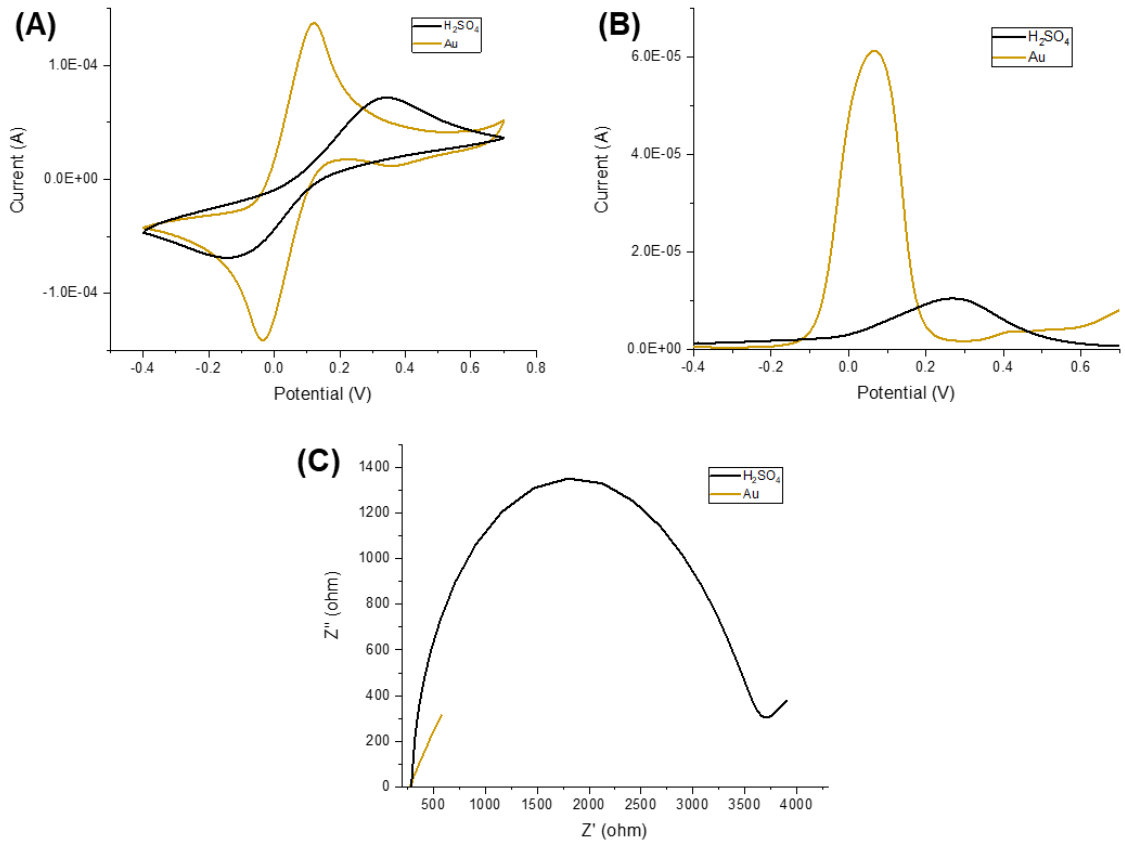

Figure 13 - Representative examples of the CV (A), SWV (B) and EIS (C) curves obtained for the electrodeposition of a NP-Au mesh by CA.

The remaining steps in the design process were followed using only EIS; MPA is a compound sensitive to electrical currents, which makes CV and SWV inadequate for this purpose [104]. Figure 14 is a representative example of the results obtained for these steps. Looking at Figure 14 one can see that the impedance and R_{ct} increase after each construction process, indicating that more non-conductive material is being added to the WE with each step. This means that the construction process was carried out successfully both in the electrodes modified with Au NPs and the electrodes modified with the NP-Au mesh. However, the final R_{ct} of the sensors modified with Au NPs is greater than the one of the sensors modified with the NP-Au mesh. At this stage, the two gold deposition techniques are no longer equivalent, but it is still too early to determine which one will perform the best. That question can only be answered once the calibration is performed, and the hybridization performance is evaluated.

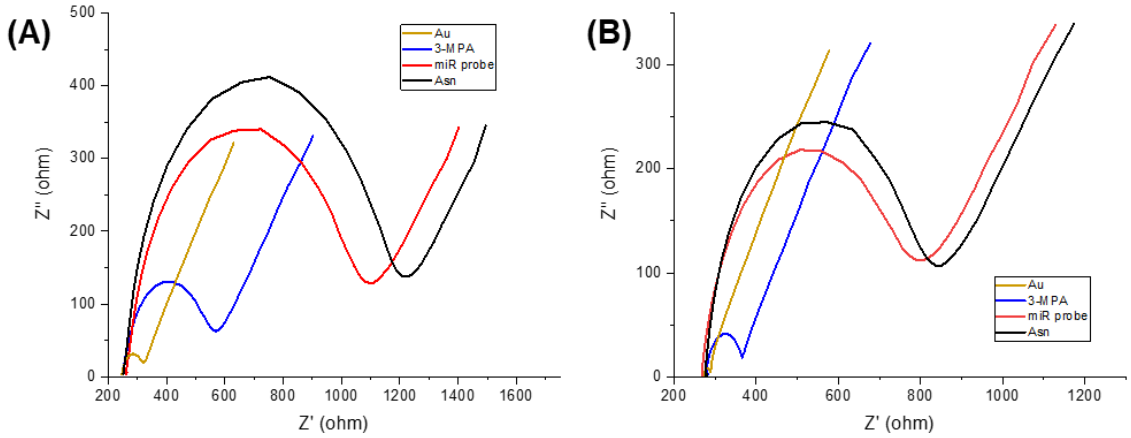

Figure 14 - Representative examples of the EIS curves obtained for the construction of the biosensors modified with Au NPs (A) and the biosensors modified with a NP-Au mesh (B). Au: gold; 3-MPA: 3-mercaptopropionic acid; miR probe: anti-miRNA-34a; Asn: L-asparagine.

3.2 - Calibration of the sensor

Hybridization Buffer selection

Calibration of the sensor was performed in three different solvents: Hybridization Buffer, FBS, and cell culture medium. Starting with the choice of Hybridization Buffer, the calibration of the sensors modified with Au NPs was performed either in phosphate buffer with 50 mM $MgCl_2$ and 150 mM NaCl, at pH=7.4 (Hybridization Buffer, pH=7.4) or in phosphate buffer with 5 mM $MgCl_2$ and 150 mM NaCl, at pH=8 (Hybridization Buffer, pH=8).

Generally, DNA and RNA hybridization are favoured by near physiological pH values and the presence of salts. At near-neutral pH (far from the pK_a of the nucleobases), the nucleobases are on a non-charged, hydrophobic state that minimizes interactions with the aqueous medium and favours interactions with the complementary sequence. Conversely, at extreme pH levels, the nucleobases become charged, hindering their ability to interact with the complementary sequences and form duplexes [105]. Optimizing the pH of the hybridization solution is, therefore, an effective strategy for promoting hybridization [106]. Another strategy for promoting hybridization is adjusting the salt concentration of the hybridization solution. The addition of cations to this solution "shiels" the negative charge of the phosphate backbone, reducing electrostatic repulsion between strands and allowing strands to bind at lower energies. To facilitate the formation of duplexes, Na^+, Li^+, K^+ and Mg^{2+} are commonly added to hybridization solutions. Mg^{2+} salts, in particular, were found to pose great influence on the hybridization rate of nucleic acid strands [105].

Figure 15 shows the results obtained for the calibration in Hybridization Buffer, pH=7.4. In Figure 15A, it is possible to see that the impedance and the R_{ct} increase after each incubation indicating that more non-conductive material is being added to the WE as the concentration of the miR-34a standards increases. Likewise, looking at Figure 15B, one can see that the current becomes smaller with each incubation, meaning that the surface is becoming less conductive as the concentration of the standards increases. Taken together, these results point to a crescent binding of miR-34a to the surface of the sensor parallel to the increase in standard concentration, which is an indication of a successful hybridization in Hybridization Buffer, pH=7.4.

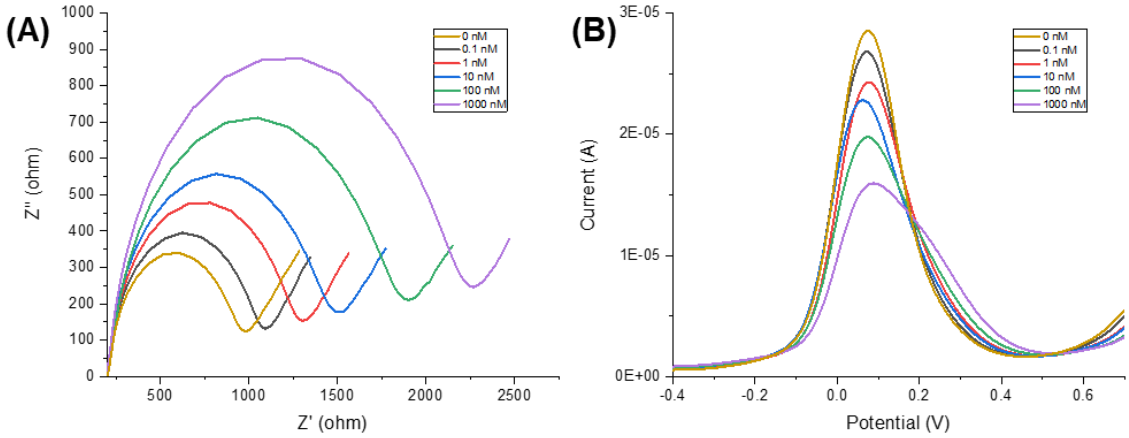

Figure 15 - Representative examples of the EIS (A) and SWV (B) curves obtained for the calibration of the biosensors modified with Au NPs. Calibration performed with miR-34a (0.1 nM – 1000 nM) in Hybridization Buffer, pH=7.4.

Using the Nova software, the R_{ct} can be extracted from the EIS curves and the I_{max} can be extracted from the SWV curves. These values can then be individually plotted against the logarithm of the concentration of the standards to yield the calibration curves in Figure 16.

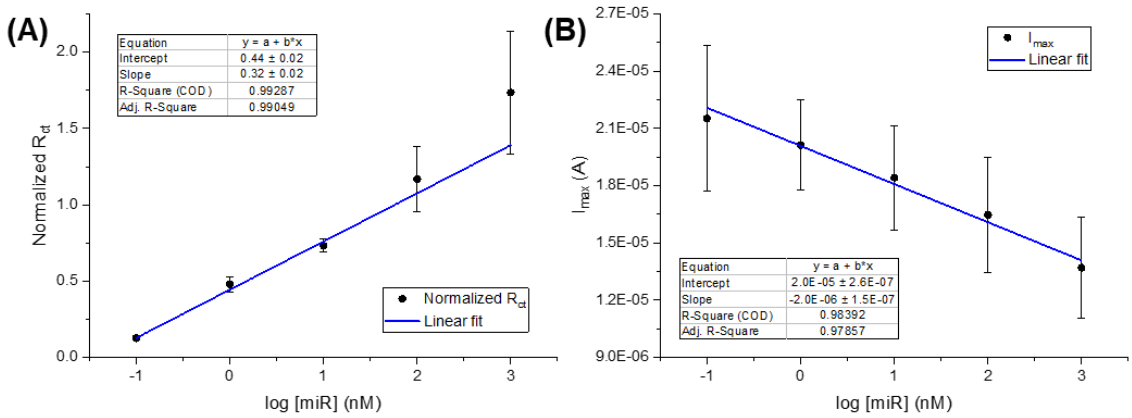

Figure 16 - Normalized R_{ct} (A) and I_{max} (B) calibration curves of the biosensors modified with Au NPs. Calibration performed with miR-34a (0.1 nM – 1000 nM) in Hybridization Buffer, pH=7.4 [1,2].

The R_{ct} calibration curve (Figure 16A) has a coefficient of determination (R^2) of 0.99287 and a slope of (0.32 ± 0.02) nM^{-1}, and it encompasses all five standards. The I_{max} calibration curve (Figure 16B) has an R^2 of 0.98392 and a slope of (-2.0 ± 0.2) $x10^{-6}$ A/nM, and it also includes all five standards. The linearity range obtained for these calibration curves is 0.1 nM to 1000 nM, which corresponds to 680 pg/mL to 6.8 µg/mL. Importantly, this range is similar to the ones obtained for other biosensing platforms designed for the detection of miR-34a [50], [57], [80].

Overall, both the EIS and SWV analysis produced a linear relationship between the logarithm of the [miR-34a] and the corresponding electrochemical parameter with a great level of confidence and accuracy. However, comparing both curves, two differences stand out: (i) the R^2 of the R_{ct} curve is higher than the one of the I_{max} curve and (ii) the error bars obtained for the R_{ct} curve are much smaller than the ones obtained for the I_{max} analysis.

[1] The error bars in all calibration curves represent standard error.

[2] Fitting of the calibration curves was performed accounting for the standard error of the points.

It is important to note that the R^2 of the calibration curves is important to assess the level of correlation between the two variables. In this work, the stringency criteria for linearity was established as R^2 higher than 0.97. On the other hand, the slope value is important to gauge accuracy since the higher the slope value is, the easier it is to distinguish two samples with similar R_{ct}/I_{max} measurements.

To determine the best analytical performance of the biosensor, the calibration process was repeated in Hybridization Buffer, pH=8. The results of the EIS and SWV analysis of this experiment are represented in Figure 17.

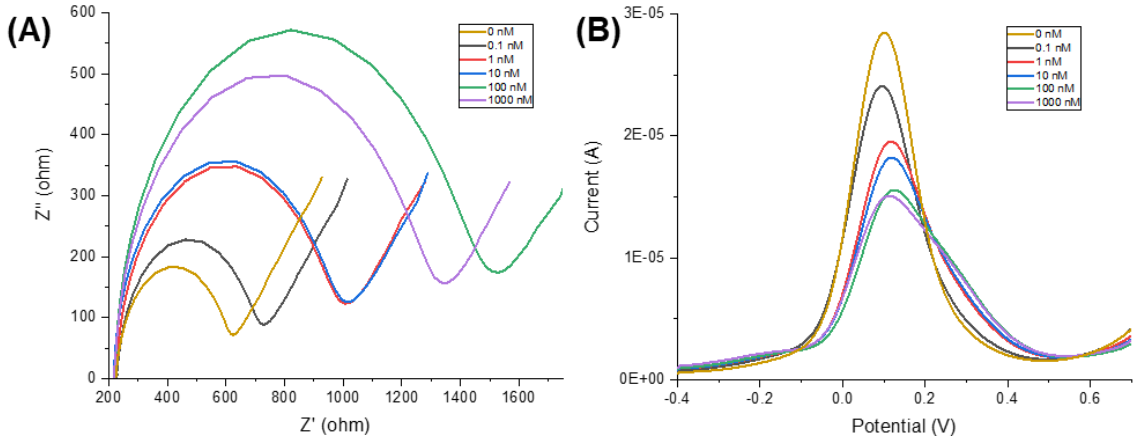

Figure 17 - Representative examples of the EIS (A) and SWV (B) curves obtained for the calibration of the biosensors modified with Au NPs. Calibration performed with miR-34a (0.1 nM – 1000 nM) in Hybridization Buffer, pH=8.

Similarly to Figure 15A, Figure 17A shows an increase in the impedance and the R_{ct} after each incubation. Likewise, both in Figure 15B and Figure 17B, one can see that the currents become smaller with each incubation. However, the jumps in-between each standard are less regular for the calibration in Hybridization Buffer, pH=8. This means that although the hybridization in Hybridization Buffer, pH=8 was successful, the calibration in this buffer might not be as successful as the one in Hybridization Buffer, pH=7.4. To confirm this suspicion, one must analyse the calibration curves in Figure 18.

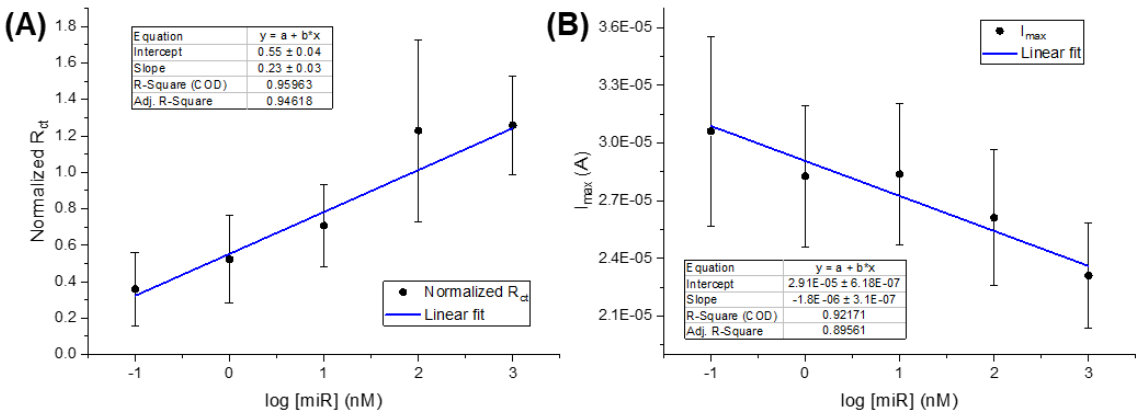

Figure 18 - Normalized R_{ct} (A) and I_{max} (B) calibration curves of the biosensors modified with Au NPs. Calibration performed with miR-34a (0.1 nM – 1000 nM) in Hybridization Buffer, pH=8.

The R_{ct} calibration curve in Figure 18A has an R^2 of 0.95963 and a slope of (0.23 ± 0.03) nM^{-1}, and it includes all five standards. Howbeit, this curve has an insufficient degree of linear

correlation between the variables since its R^2 is lower than 0.97. Compared to the R_{ct} calibration curve in Hybridization Buffer, pH=7.4 (Figure 16A), this curve has a lower R^2 (in fact, below the linearity stringency criteria) and a lower slope value.

The I_{max} calibration curve in Figure 18B has an R^2 of 0.92171 and a slope of (-1.8 ± 0.3) x10^{-6} A/nM nM^{-1}, and it encompasses all five standards. However, this curve also presents an insufficient linear correlation between the variables since it has an R^2 lower than 0.97. Compared to the I_{max} calibration curve in Hybridization Buffer, pH=7.4 (Figure 16B), this curve has a lower R^2.

Comparing both curves in Hybridization Buffer, pH=8, the R^2 of the R_{ct} curve is once again higher than that of the I_{max} curve, and the error bars obtained for the R_{ct} are smaller than the ones obtained for the I_{max} analysis. Thus, even though EIS and SWV are equally valid and interchangeable techniques for the analysis of the hybridization process, only EIS analysis will be performed moving forward because it yields better results.

Overall, comparing the hybridization performance between the two buffers, the R^2 is consistently lower for the calibration in Hybridization Buffer, pH=8. Moreover, both in the R_{ct} and the I_{max} curves, the error bars are smaller for the calibration in Hybridization Buffer, pH=7.4 than for the calibration in Hybridization Buffer, pH=8. The first takeaway from this comparison is that the calibration in these buffers is not equivalent, meaning that the variations in pH and salt concentration did affect the hybridization performance. In this case, the hybridization appears to be favoured by physiological pH values (pH=7.4) as well as by the presence of a higher concentration of Mg^{2+} salts. The second finding is that the calibration in Hybridization Buffer, pH=7.4 yielded better results than the calibration in Hybridization Buffer, pH=8. Thus, the Hybridization Buffer, pH=7.4 was determined as the Hybridization Buffer to be used in the remaining assays.

Gold deposition technique selection

To understand which gold deposition technique shows the best analytical performance, the calibration of each type of sensor was performed in Hybridization Buffer, pH=7.4. The results obtained for the calibration of the sensors modified with Au NPs were already analysed in the previous subsection and are summarized in Figure 15 and Figure 16. The results of the EIS analysis of the calibration process of the sensors modified with the NP-Au mesh are represented in Figure 19.

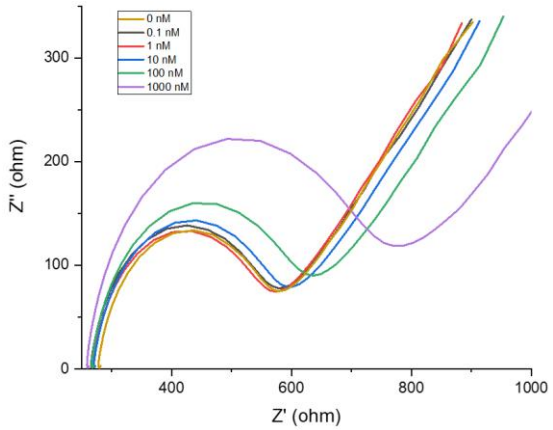

Figure 19 - Representative example of the EIS curves obtained for the calibration of the biosensors modified with a NP-Au mesh. Calibration performed with miR-34a (0.1 nM – 1000 nM) in Hybridization Buffer, pH=7.4.

Once again, the EIS analysis (Figure 19) showed an increase in the impedance and the R_{ct} after each incubation, indicating that hybridization was successful. However, the jumps in-between standards were less regular and, in most cases, less pronounced than the ones in Figure 15A (biosensors modified with Au NPs), which might indicate that the hybridization performance is favoured by the modification with Au NPs. It is also noteworthy to mention that the impedance was consistently higher on the sensors modified with Au NPs.

To further distinguish the two methods of gold deposition, the results were converted into the calibration curves in Figure 20.

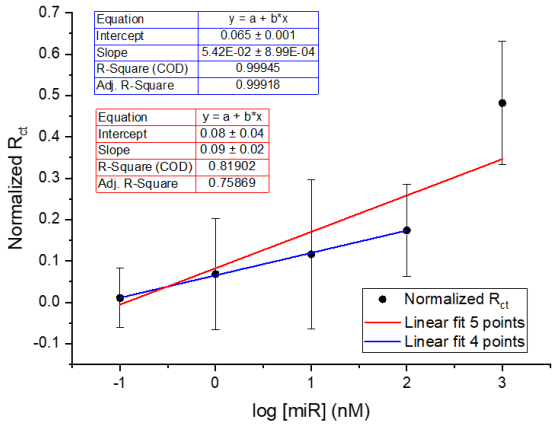

Figure 20 - Normalized R_{ct} calibration curves of the biosensors modified with a NP-Au mesh. Calibration performed with miR-34a (0.1 nM – 1000 nM) in Hybridization Buffer, pH=7.4.

Figure 20 shows two attempts at fitting the data into a linear curve. The red line has an R^2 of 0.81902 and a slope of (0.09 ± 0.02) nM^{-1}, and it encompasses all five standards. The blue line has an R^2 of 0.99945 and a slope of (0.0542 ± 0.0009) nM^{-1}, but it only includes four standards (the standard with the highest concentration was left out). Overall, the red curve has a lower R^2 but a higher slope. However, since this curve has an R^2 below the linearity stringency criteria, only the blue curve will be used for comparing the gold deposition techniques.

Comparing the curve in Figure 16A (Au NPs) with the blue curve in Figure 20 (NP-Au mesh), it is clear that, although the R^2 values are similar (0.99287 vs 0.99945, respectively), the slope value of the Au NPs curve is almost 10-fold higher than the one of the NP-Au mesh curve (0.32 ± 0.01 vs 0.0542 ± 0.0009, respectively). That means that the biosensors modified with Au NPs yielded more accurate curves than the sensors modified with the NP-Au mesh, indicating that the morphology of the NPs might be more favourable for hybridization than the morphology of the meshes. One possible explanation for this observation is the fact that the NPs may provide a curvier surface (with a higher surface-to-volume ratio) for the attachment of the miRNA probes, allowing them to be further apart and reducing the steric hindrance of hybridization [106]. However, this supposition needs to be confirmed; more accurate conclusions could be drawn after characterization of the morphology of the surface, for example, through scanning electron microscopy (SEM).

Overall, the sensors modified with Au NPs appear to have a better hybridization performance than the ones modified with the NP-Au mesh and, thus, will be exclusively addressed from this point onward. In the future, it would be interesting to evaluate the influence of the size and shape of the Au NPs on the sensor's performance. Perhaps a different

type of gold nanostructures (e.g., nanostars or nanorods) or a different deposition technique (e.g., drop-casting) will lead to an even better performance of sensor, lowering its LOD.

Calibration in serum

After selecting the most appropriate gold deposition technique and hybridization buffer, the hybridization performance of the sensor was put through a more stringent test. For that, filtered and diluted FBS was used to prepare the miR-34a standard solutions. The initial idea was to simply dilute the FBS in Hybridization Buffer (on a 1:100 proportion) to adjust its pH to 7.4. However, some compounds in the unfiltered FBS were negatively interacting with the sensor, hampering its linear response (results not shown). To try to correct this problem, the diluted FBS was filtered using a centrifugal unit with a 100 kDa filter. The 100 kDa cut-off allows the removal of several compounds in serum (mostly proteins), while retaining free-floating cimiRNAs (such as miR-34a) in solution [60]. This procedure restored the linear response of the sensor, which will now be discussed. The EIS analysis of the calibration in filtered and diluted FBS is represented in Figure 21.

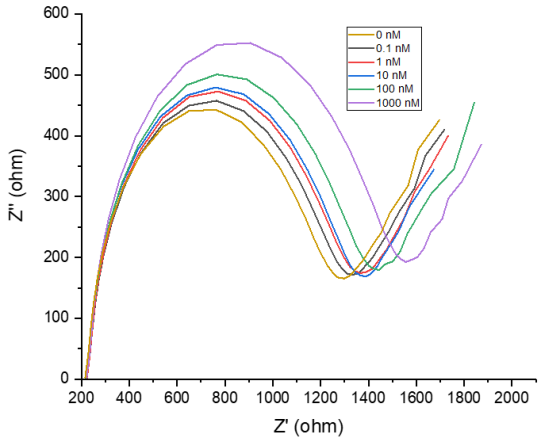

Figure 21 - Representative example of the EIS curves obtained for the calibration of the biosensors modified with Au NPs. Calibration performed with miR-34a (0.1 nM – 1000 nM) in filtered and diluted FBS (1:100 in Hybridization Buffer, pH=7.4).

From Figure 21, one can see that the impedance and the R_{ct} increase linearly with the increase in miR-34a concentration, despite doing so in a less evident trend than in Figure 15A (calibration in Hybridization Buffer, pH=7.4). This difference is also visible on the R_{ct} calibration curve in Figure 22. The curve in Figure 22 has an R^2 of 0.98555 and a slope of (0.037 ± 0.003) nM^{-1}, and it includes all five standards. Despite being within the limits of linearity, the R^2 is slightly lower and, most importantly, the slope is around 10-fold lower than the one in Figure 16A (0.037 ± 0.003 vs 0.32 ± 0.01, respectively). Nevertheless, the curve obtained for the calibration in FBS is still accurate and reliable, and the reduction in slope value is easily justifiable by the increase in medium complexity. In the future, a filter with a smaller pore diameter might be used to try to filter out more interferents and improve this value.

In any case, it is worth noting that the linearity range obtained for this calibration (0.1 nM to 1000 nM) is similar to the ones obtained for other biosensing platforms designed for the detection of miR-34a [50], [57], [80].

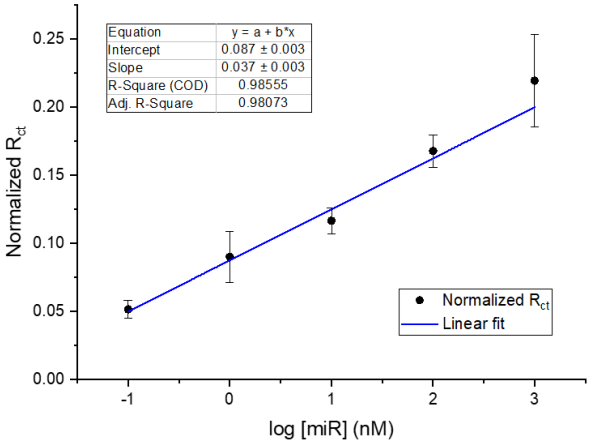

Figure 22 - Normalized R_{ct} calibration curve of the biosensors modified with Au NPs. Calibration performed with miR-34a (0.1 nM – 1000 nM) in filtered and diluted FBS (1:100 in Hybridization Buffer, pH=7.4).

Calibration in cellular medium

Envisioning the application of the biosensor for the analysis of cultured cells, the calibration of the biosensor was also performed in cell culture medium (Differentiation Medium). In line with the experiments in FBS, the cell culture medium was firstly diluted in Hybridization Buffer (1:100 dilution) and then filtered, as previously explained. The filtration was done as a pre-emptive measure because interference was predictable due to the presence of 1% FBS on the cell culture medium. The EIS results of the calibration in cell culture medium are represented in Figure 23.

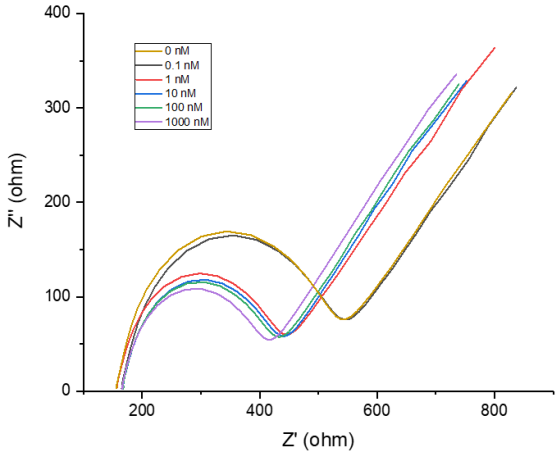

Figure 23 - Representative example of the EIS curves obtained for the calibration of the biosensors modified with Au NPs. Calibration performed with miR-34a (0.1 nM – 1000 nM) in filtered and diluted cell culture medium (1:100 in Hybridization Buffer, pH=7.4).

In contrast with the two previous calibrations in Figure 15A (Au NPs, Hybridization Buffer) and in Figure 21 (Au NPs, FBS), Figure 23 shows a reduction in impedance and R_{ct} after each incubation. These variations are smaller, less uniform, and descending; nonetheless, a trend remains. Although unusual, this result is not indicative of a malfunction of the system but rather of the presence of additional interfering substances which alter the electrical response of the electrodes. This change is even more evident in the R_{ct} calibration curve in Figure 24.

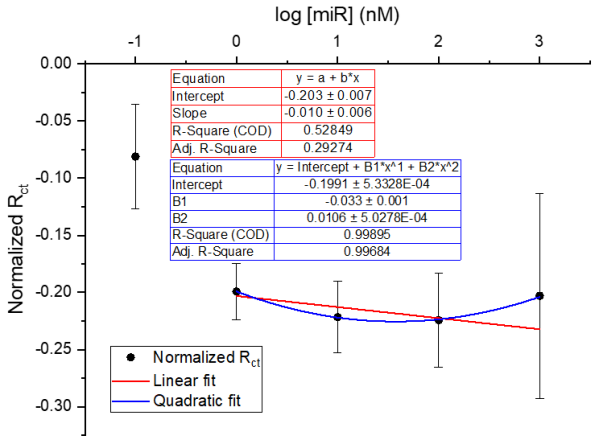

Figure 24 - Normalized R_{ct} calibration curve of the biosensors modified with Au NPs. Calibration performed with miR-34a (0.1 nM – 1000 nM) in filtered and diluted cell culture medium (1:100 in Hybridization Buffer, pH=7.4).

Looking at Figure 24, it is evident that, even after removing the miR-34a standard with the lowest concentration (which is clearly outside the limits of linearity), the sensor does not exhibit a linear response. The linear curve in Figure 24 (red) has an R^2 of only 0.52849, far below the linearity stringency criteria. However, the quadratic curve in Figure 24 (blue) has an R^2 of 0.99895. The R^2 of this quadratic curve shows an acceptable degree of correlation between the logarithm of the [miR-34a] and the normalized R_{ct} values. Nonetheless, the quadratic relationship is not ideal because it is more complicated to compute and it yields two solutions, leaving the user to find the one closest to reality.

Overall, this experiment had only moderate success, producing a reliable calibration curve in cell culture medium but failing to do so in a linear manner. As previously mentioned, this is likely the result of the interaction of some components of the cell culture medium with the surface of the sensor. The cell culture medium is a complex matrix and may require further filtrations (or, alternatively, filtrations with smaller pore diameter filters) to remove the compounds that interfere with the biosensor. Optimizing these conditions may help to not only obtain a linear relationship between the logarithm of the [miR-34a] and the normalized R_{ct} values, but also to lower the LOD of the biosensor.

3.3 - Specificity/selectivity tests

To assess the specificity/selectivity of the biosensor, its response was evaluated in the presence of potentially interfering substances. Two substances found in human plasma were tested as potential interferents: creatinine and miR-107. Both biomolecules have low molecular weights, which ensures they will be retained in solution after filtration.

Creatinine was chosen because it is a commonly analysed biomolecule, whose serum levels are fairly constant. In healthy patients, these levels range from 45-90 µM for women and from 60–110 µM for men [107]. Thus, the serum concentration of creatinine was approximated to 90 µM. On the other hand, miR-107 was chosen as a way of testing the affinity of the biosensor for other nucleic acid sequences. According to *Carneiro et al.*, miR-107 is detectable within a concentration range of 1 pM to 1 µM [71]. Since the miR-107 sequence has a DNA nature, its binding to the sensor is favoured in comparison to the mimetic miR-34a sequence (of RNA nature). Therefore, the miR-107 serum concentration was defined as 1 pM to mitigate this

disparity. Considering their plasma concentration and the FBS dilution performed in the previous subsection, the miR-107 concentration was set to 10 fM and the creatinine concentration was set to 900 nM.

Figure 25 shows the deviation in R_{ct} variation caused by the addition of miR-107 or creatinine to the 0.1 nM miR-34a standard solution. From the graph in Figure 25, one can see that the addition of miR-107 caused a small deviation in the sensor's response of 10.1% regarding the miR-34a standard solution, and the addition of creatine caused a similar deviation of 11.3%. Nonetheless, the deviation in both cases is within the usual limits of acceptability, meaning that these two substances do not significantly interfere with the sensor's response. Thus, under the conditions tested, the sensor demonstrated specificity/selectivity for miR-34a.

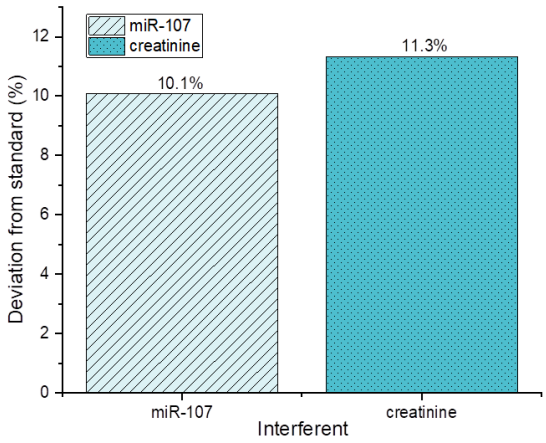

Figure 25 - Deviation on the R_{ct} standard variation caused by the addition of miR-107 or creatinine. Standard solution made up of 0.1 nM miR-34a in Hybridization Buffer, pH=7.4.

3.4 - *In vitro* proof of concept

Neuronal differentiation

To verify if the neuronal differentiation protocol (involving decrease in FBS concentration and RA exposure) was successful, and if the addition of the neurotoxicant 6-OHDA to the media produced a significant effect on the cells, the cells were observed under a bright-field microscope prior to fixation (i.e., 5 days after culturing, including 1 day under stimulation with 6-OHDA). Figure 26 contains representative images of each condition (Non-DIFF, DIFF_0, DIFF_50, and DIFF_100) at this time. The most evident conclusion one can take from Figure 26 is that the Non-DIFF cells (Figure 26A) have a critically different morphology from the DIFF cells (Figure 26B-D). The DIFF cells have a more spread-out morphology and present a perceptible increase in neurite-like extensions in comparison to the non-differentiated cells. Both of these characteristics are frequently associated to the differentiation of SH-SY5Y cells into a more mature neuronal-like state and have been previously reported by many authors, including *Simões et al.* [41]. It is also important to note that the Non-DIFF cells showed more propension to aggregate in clusters, and that the cell density 5 days after platting is similar across all conditions. Considering that the Non-DIFF cells were seeded at a much lower concentration, this observation indicates that the Non-DIFF cells proliferated at a different rate than the DIFF cells. Moreover, it indicates that the DIFF cells stopped dividing, similarly to the mature neuronal cells *in vivo*. Since the pause in proliferation is a hallmark of differentiation [40], one

can conclude that the addition of RA to the medium was capable of inducing neuronal differentiation.

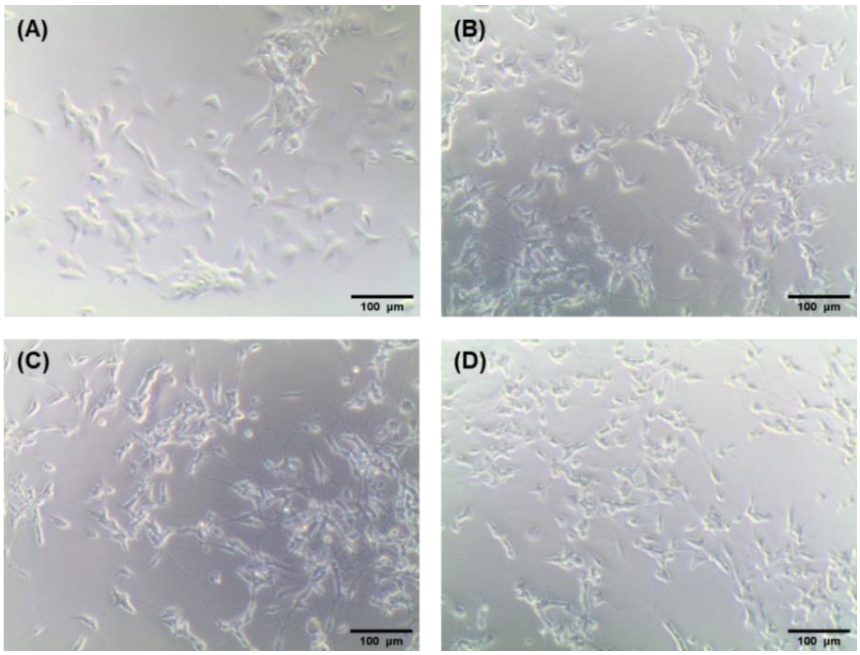

Figure 26 – Representative images of the bright-field observation of the Non-DIFF (A), DIFF_0 cells (B), DIFF_50 (C), and DIFF_100 (D) cells, 5 days after platting.

There are also morphological differences between the DIFF cells, although more subtle. Looking at Figure 26B-D, the cellular bodies of the neuronal-like cells in the DIFF_100 well (Figure 26D) seem to be smaller than the ones in the DIFF_0 (Figure 26B) and DIFF_50 (Figure 26C) wells. Likewise, this condition appears to have more round cells than the other two differentiated conditions. Cytoplasmatic condensation and cell rounding are two hallmarks of apoptosis [108] and may indicate that these cells are undergoing cellular death due to the exposure to 6-OHDA. In any case, the difference in cellular morphology is greater between the DIFF_0 and DIFF_100 conditions than between the DIFF_0 and DIFF_50 conditions. This indicates that the effect of 6-OHDA might be concentration dependent and become more pronounced as the concentration increases.

Overall, it can be concluded from this assay that the exposure to RA drove the cells towards a more neuronal-like phenotype and that the addition of the neurotoxic compound 6-OHDA to the media affected the morphology and viability of the cells. This effect was particularly noticeable on the cells exposed to the highest concentration of 6-OHDA (DIFF_100 cells).

Immunocytochemistry

To better understand the effects of differentiation and exposure to 6-OHDA on the cells, they were subjected to immunocytochemical assays. ß-tubulin III, a microtubule element almost exclusively found in neurons, was stained by an anti-ß-tubulin III primary antibody followed by a secondary antibody fluorescently labelled with Alexa Fluor 488; the nuclei were stained using DAPI and the F-actin was stained with Flash Phalloidin™ Red 594. The samples were then visualized using fluorescence microscopy. Representative images of the observations made are shown in Figure 27.

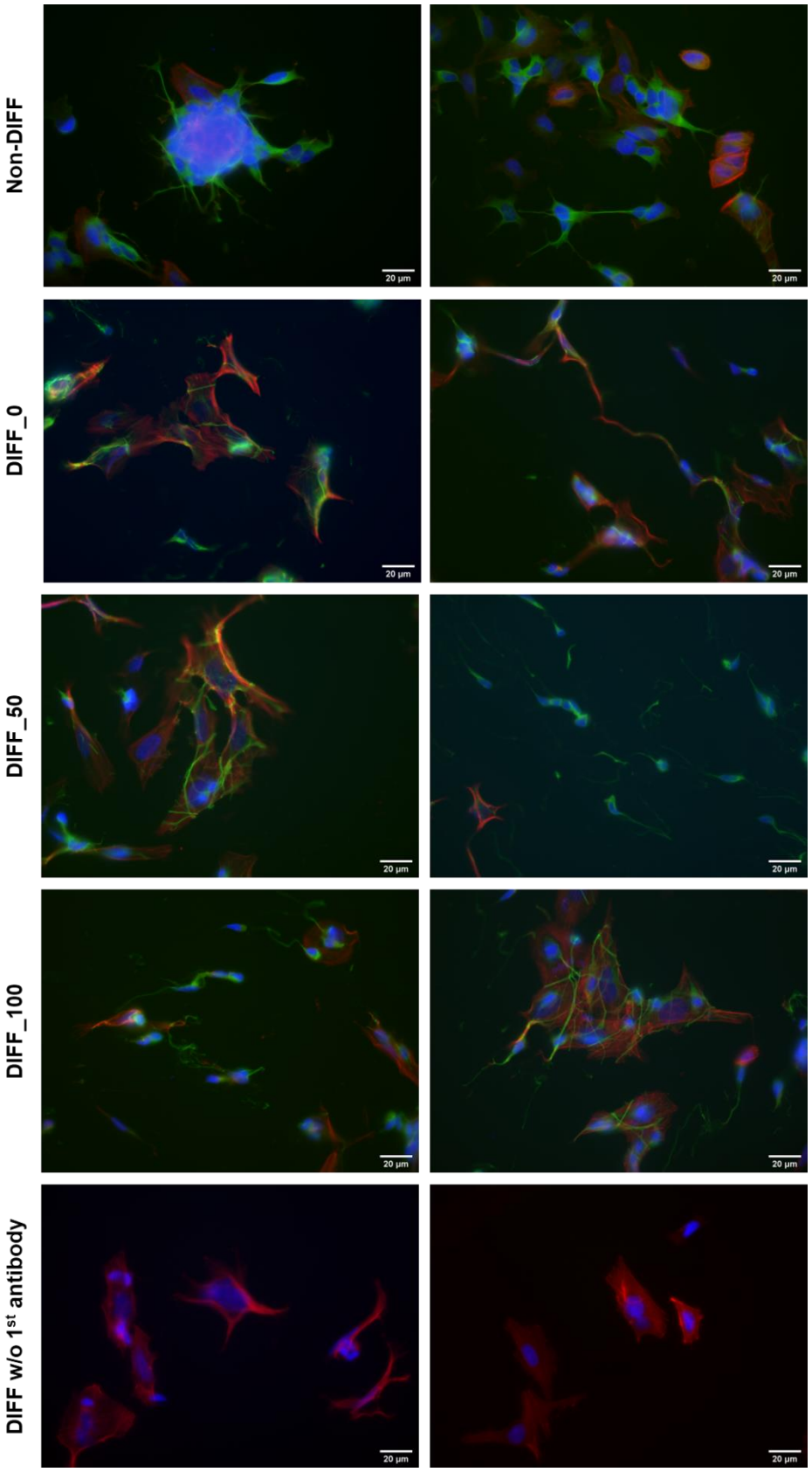

Figure 27– Representative images of observation of the cells under the fluorescence microscope. Green represents ß-tubulin III, blue the nuclei and red F-actin.

The first observation from Figure 27 is that the ß-tubulin III staining was performed correctly because no green signal can be detected on the samples without the primary antibody (DIFF w/o 1st antibody). The second observation is that ß-tubulin III can be detected in all conditions. At first glance, seeing non-differentiated cells expressing ß-tubulin III may seem rather strange because ß-tubulin III expression is usually associated with mature neurons [41]. However, undifferentiated SH-SY5Y cells can express immature neuronal biomarkers [33], including ß-tubulin III [109]. In fact, this phenomenon has already been reported by other authors, like *Murillo et at*. [40]. Thus, although unexpected, this observation is simply a characteristic of the cell line in use.

Inspecting the ß-tubulin III expression more deeply, one can see that even though this biomarker is present in both types of wells (DIFF and Non-DIFF) its spatial expression is not equivalent. In Non-DIFF wells, the signal for ß-tubulin III is more evenly distributed within the cellular body whereas, in DIFF wells, this signal is usually confined to thin lines that wrap around the cells. This indicates a higher level of microtubule organization within the cells exposed to RA (possibly associated with the formation of neurites), which agrees with the bright-field observation (Figure 26) that cells exposed to RA present a visible increase in neurite-like processes. Also in agreement with the bright-field observations is the presence of a similar quantity of nuclei across all conditions (excluding the cluster on the left image of the Non-DIFF condition), albeit their different plating densities. Once again, this is an indication that the exposure to RA stopped proliferation.

In general, all the images on Figure 27 possess cells with a differentiated morphology in simultaneous with cells with an undifferentiated morphology. Nonetheless, the relative proportion of differentiated cells is much larger on the wells exposed to RA. This means that although the exposure to RA was successful at inducing differentiation, some cells retained an undifferentiated morphology.

Looking at the morphology of the nuclei, the Non-DIFF condition appears to have rounder, brighter and smaller nuclei than the DIFF conditions. Comparing the DIFF conditions, the DIFF_50 and DIFF_100 conditions have an increase in this type of condensed nuclei compared to the DIFF_0. Rather than being an indication of insufficient differentiation, this may represent a pyknotic nuclei observation, which indicates that the cells are undergoing apoptotic nuclear condensation due to 6-OHDA exposure. This behaviour was already noted on the bright-field images and has already been observed in other works, such as the one by *Rehfeldt et al*. [110].

Finally, analysing the phalloidin staining, the F-actin filaments appear to be more organized on the DIFF conditions rather than the Non-DIFF condition. This is in accordance with all previous observations of RA-induced differentiation and is a confirmation of the success of the differentiation protocol.

Altogether, the fluorescence observations corroborated the bright-field observations: RA induced a neuronal-like phenotype on the SH-SY5Y cells and 6-OHDA appears to have an apoptotic effect on these cells, howbeit, more visible in bright-field analysis.

Testing the sensor in cellular media extracts

To further validate the applicability of the biosensor herein described, the cellular media were analysed. Firstly, the sensors were stabilized in filtered and diluted Differentiation Medium (1:100 in Hybridization Buffer) that had been incubated in an empty well, in parallel with the cell culture wells. Afterwards, each sensor received a sample of one of the conditions

tested – DIFF_0, DIFF_50 or DIFF_100 -, also filtered and diluted (1:100 in Hybridization Buffer). Figure 28 shows the shift in the impedance caused by the addition of each of these samples.

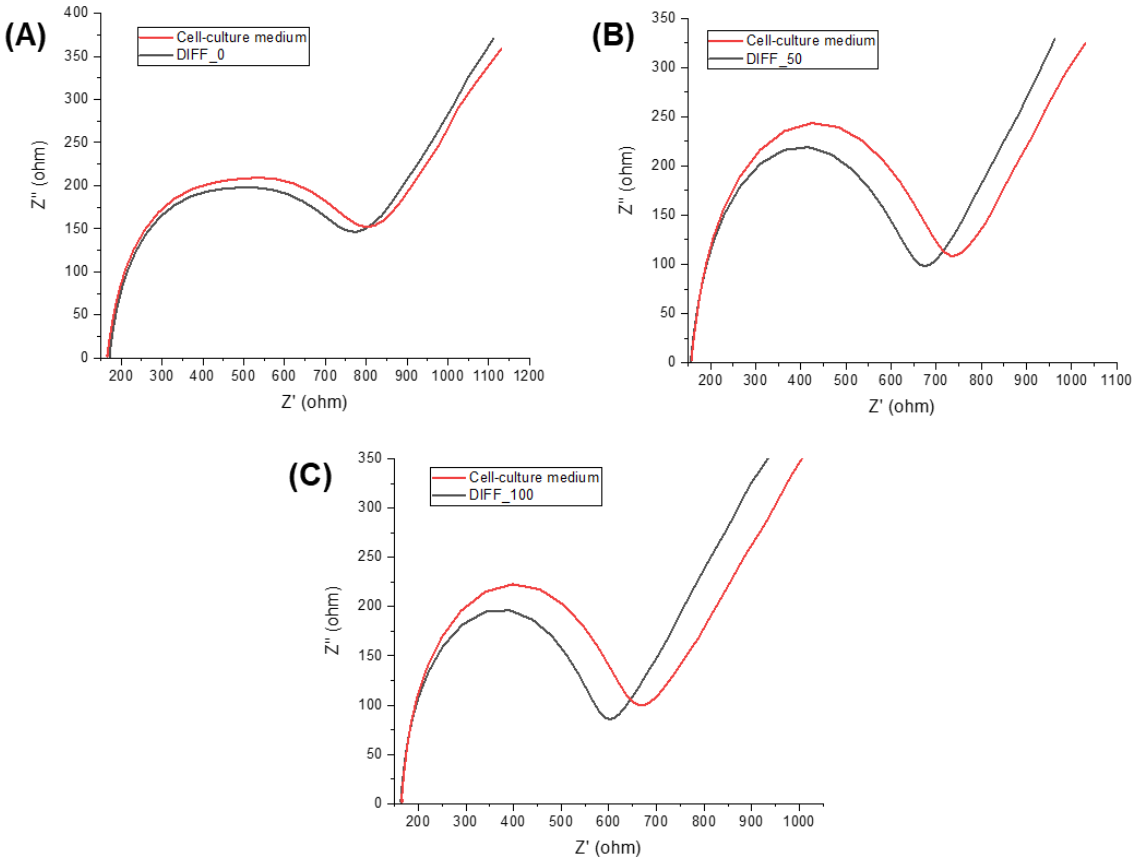

Figure 28- EIS curves obtained for the incubation of cellular media extracts on the biosensors modified with Au NPs. Stabilization in filtered and diluted cell culture medium (1:100 in Hybridization Buffer). Incubation in filtered and diluted (1:100 in Hybridization Buffer) samples of the DIFF_0 (A), DIFF_50 (B), and DIFF_100 (C) conditions.

The first conclusion to draw from the results on Figure 28 is that the addition of the samples caused a shift in the EIS curve, which indicates that there was miR-34a in the cellular media. The second conclusion is that this variation seems greater on the DIFF_50 sample (Figure 28B) than on the DIFF_0 sample (Figure 28A), and even greater on the DIFF_100 sample (Figure 28C), suggesting that the concentration of miR-34a augments proportionally to the increase in 6-OHDA concentration. This is an exciting result because it not only corroborates the observations made on the two previous subsections, but also indicates that the stimulation of miR-34a excretion by 6-OHDA was successful.

Uplifted by these results, the variation in R_{ct} caused by the samples was compared against the calibration curve in Figure 24 to try to estimate the concentration of miR-34a. It is worth noting that the calibration curve was designed using a mimetic miR-34a sequence, of DNA nature. Thus, the estimated results may not be as reliable as they could, since the miR-34a present in the cell culture media is of RNA nature. Table 1 represents this variation in R_{ct} as well as the two concentrations calculated using the calibration curve on Figure 24 (Norm R_{ct} = -0.199 - 0.033 log[miR] + 0.011 log[miR]^2). Looking at Table 1, one can see that the absolute value of the normalized R_{ct} becomes larger as the concentration of 6-OHDA increases. Unfortunately, the calculated values of [miR-34a] are outside the bounds of the calibration curve, i.e., the lowest calculated concentration (2.19 pM) is smaller than the lowest standard

of the calibration curve (1 nM) and the highest calculated concentration (456.33 μM) is larger than the highest standard of the calibration curve (1 μM). Thus, the calculated values are highly unreliable, meaning that no further insights were gained from this analysis.

Table 1 - Variation in R_{ct} caused by the incubation of cellular media extracts on the sensors and their corresponding calculated concentrations.

Condition	Norm R_{ct}	Calculated [miR] (pM)	Calculated [miR] (μM)
DIFF_0	-0.03345	2.19	456.33
DIFF_50	-0.08768	9.61	104.03
DIFF_100	-0.12327	30.04	33.29

In conclusion, this test pointed to a correct stimulation of miR-34a secretion by 6-OHDA, which seems to be concentration-dependent. However, the calibration curve was not sufficiently broad to allow the confirmation of this observation nor to quantify the miRNA concentration of the samples. In the future, a broader calibration curve should be designed for this purpose. Ideally the calibration curve should also be designed with the real RNA sequence of miR-34a, not the mimetic sequence (of DNA nature) herein used. Likewise, the increase in miR-34a secretion should be confirmed by an already well-established quantification technique, such as a TaqMan™ MicroRNA Assay. This is a technique specially designed to detect and quantify mature miRNAs. miRNAs are too small to be quantified through the conventional random-primed reverse transcription real-time PCR techniques. To overcome this problem, the TaqMan™ MicroRNA Assay uses target-specific stem-looped primers for the reverse transcription of miRNAs. This creates longer reverse transcription products that can be used as templates for real-time PCR using TaqMan™ assays [111], [112].

In summary, this section confirmed that the construction process of the biosensor was successful (independently of the gold deposition technique used), and that it allowed the detection of miR-34a. It also showed that the hybridization between the target and the probe was favoured by the modification with Au NPs and by the use of the Hybridization Buffer, pH=7.4. Moreover, it demonstrated that, under these circumstances, the biosensor successfully detects miR-34a in FBS, cell culture medium and in the presence of potential interferents. In fact, the sensor was able to detect miR-34a within a linear range of 100 pM to 1 μM (both in buffer and in serum), similarly to other miR-34a biosensors. Lastly, it proved that the cellular protocols used had the desired results and that the sensor demonstrates great potential to be used for the analysis of cellular media extracts.

Chapter 4

Conclusion and outlook

Throughout the previous chapters, the reader was guided through the journey of the development of a miRNA-based electrochemical sensor for the detection of AD. This journey began by contextualizing the tremendous societal impact of this disease and by presenting the motivation for this work: the dire need for new, less-invasive and, ideally, early-stage diagnostic tools for AD. It continued with the reasoning behind the choice of a gold-modified, anti-miR-34a-based C-SPE to achieve this goal. The gold nanostructures increase the sensitivity of the inexpensive C-SPEs while providing a greater surface area for its modification with the oligonucleotide probe. The anti-miR-34a makes a highly selective biomolecular probe, which is capable of binding to a potential AD blood biomarker of increasing reliability – miR-34a.

Keeping this design in mind, a set of experiments was laid out to develop and test the proposed biosensor. In summary, this biosensor was able to successfully detect miR-34a in hybridization buffer and in serum, within a linear range of 100 pM to 1 μM, which is similar to the ones obtained for previously designed miR-34a biosensing platforms. Furthermore, the sensor was successful at identifying miR-34a in biological samples, demonstrating that the design developed holds great promise for the application in a real scenario.

Although this work lays an exceptional foundation for the development of a new AD diagnostic tool, many steps must be taken before the sensor is used in clinical practice. First and foremost, the hybridization performance of the biosensor must be optimized to lower the LOD of the sensor. Keeping a POC approach in mind, this could be done by tweaking the construction process of the sensor or by changing the hybridization buffer. For example, the Au NPs could be fabricated by drop-casting instead of electropolymerization, or they could be replaced by other gold nanostructures, such as gold nanostars or nanorods, to try to optimize the LOD of the sensor. Secondly, more stringent specificity and selectivity tests will need to be performed, by calibrating the sensor in the presence of other serum components and microRNAs (e.g., a scrambled miR-34a sequence). Thirdly, the stability of the sensor will need to be determined and possibly optimized. Fourthly, the sensor must be tested in plasma, using human samples (both of AD patients and healthy controls), and the clinical validity of this assay must

be assured. The biosensor can also be tested in transgenic mice models beforehand, to fine-tune the design of the sensor in a biological context similar to the clinic, before validating it in expensive and cumbersome clinical trials.

Overall, the work herein presented demonstrated that miRNA-based sensors (in particular, those based on miR-34a) have great potential for the clinical detection of AD. In the future, they may arise as cheaper and less-invasive alternatives to the currently available diagnostic methods, revolutionizing the landscape of AD diagnosis. Optimistically, the introduction of such platforms will facilitate the access of many patients to a diagnosis, empowering them to seek prompt treatment and extending their quality of life.

References

[1] Z. Breijyeh and R. Karaman, 'Comprehensive Review on Alzheimer's Disease: Causes and Treatment', *Molecules*, vol. 25, no. 24, p. 5789, Dec. 2020, doi: 10.3390/molecules25245789.

[2] G. Cipriani, C. Dolciotti, L. Picchi, and U. Bonuccelli, 'Alzheimer and his disease: a brief history', *Neurol. Sci.*, vol. 32, no. 2, pp. 275–279, Apr. 2011, doi: 10.1007/s10072-010-0454-7.

[3] M. W. Bondi, E. C. Edmonds, and D. P. Salmon, 'Alzheimer's Disease: Past, Present, and Future', *J. Int. Neuropsychol. Soc. JINS*, vol. 23, no. 9–10, pp. 818–831, Oct. 2017, doi: 10.1017/S135561771700100X.

[4] T. F. Ahmed, A. Ahmed, and F. Imtiaz, 'History in perspective: How Alzheimer's Disease came to be where it is?', *Brain Res.*, vol. 1758, p. 147342, May 2021, doi: 10.1016/j.brainres.2021.147342.

[5] C. Ferrari and S. Sorbi, 'The complexity of Alzheimer's disease: an evolving puzzle', *Physiol. Rev.*, vol. 101, no. 3, pp. 1047–1081, Jul. 2021, doi: 10.1152/physrev.00015.2020.

[6] M. M. J. van den Berg, J. Krauskopf, J. G. Ramaekers, J. C. S. Kleinjans, J. Prickaerts, and J. J. Briedé, 'Circulating microRNAs as potential biomarkers for psychiatric and neurodegenerative disorders', *Prog. Neurobiol.*, vol. 185, p. 101732, Feb. 2020, doi: 10.1016/j.pneurobio.2019.101732.

[7] Y. Zhao, Y. Zhang, L. Zhang, Y. Dong, H. Ji, and L. Shen, 'The Potential Markers of Circulating microRNAs and long non-coding RNAs in Alzheimer's Disease', *Aging Dis.*, vol. 10, no. 6, pp. 1293–1301, Dec. 2019, doi: 10.14336/AD.2018.1105.

[8] W. Wong, 'Economic burden of Alzheimer disease and managed care considerations', *Am. J. Manag. Care*, vol. 26, no. 8 Suppl, pp. S177–S183, Aug. 2020, doi: 10.37765/ajmc.2020.88482.

[9] A. Villarejo Galende, M. Eimil Ortiz, S. Llamas Velasco, M. Llanero Luque, C. López de Silanes de Miguel, and C. Prieto Jurczynska, 'Report by the Spanish Foundation of the Brain on the social impact of Alzheimer disease and other types of dementia', *Neurol. Engl. Ed.*, vol. 36, no. 1, pp. 39–49, Jan. 2021, doi: 10.1016/j.nrleng.2017.10.004.

[10] Alzheimer's Association, '2021 Alzheimer's disease facts and figures', *Alzheimers Dement.*, vol. 17, no. 3, pp. 327–406, 2021, doi: 10.1002/alz.12328.

[11] M. Moraghebi, R. Maleki, M. Ahmadi, A. A. Negahi, H. Abbasi, and P. Mousavi, 'In silico Analysis of Polymorphisms in microRNAs Deregulated in Alzheimer Disease', *Front. Neurosci.*, vol. 15, p. 631852, 2021, doi: 10.3389/fnins.2021.631852.

[12] D. Galimberti *et al.*, 'Circulating miRNAs as potential biomarkers in Alzheimer's disease', *J. Alzheimers Dis. JAD*, vol. 42, no. 4, pp. 1261–1267, 2014, doi: 10.3233/JAD-140756.

[13] K. G. Yiannopoulou and S. G. Papageorgiou, 'Current and Future Treatments in Alzheimer Disease: An Update', *J. Cent. Nerv. Syst. Dis.*, vol. 12, p. 1179573520907397, Jan. 2020, doi: 10.1177/1179573520907397.

[14] S. Hu, C. Yang, and H. Luo, 'Current trends in blood biomarker detection and imaging for Alzheimer's disease', *Biosens. Bioelectron.*, vol. 210, p. 114278, Aug. 2022, doi: 10.1016/j.bios.2022.114278.

[15] S. Khan, K. H. Barve, and M. S. Kumar, 'Recent Advancements in Pathogenesis, Diagnostics and Treatment of Alzheimer's Disease', *Curr. Neuropharmacol.*, vol. 18, no. 11, pp. 1106–1125, 2020, doi: 10.2174/1570159X18666200528142429.
[16] Y. H. El-Hayek *et al.*, 'Tip of the Iceberg: Assessing the Global Socioeconomic Costs of Alzheimer's Disease and Related Dementias and Strategic Implications for Stakeholders', *J. Alzheimers Dis.*, vol. 70, no. 2, pp. 323–341, Jan. 2019, doi: 10.3233/JAD-190426.
[17] J. Penney, W. T. Ralvenius, and L.-H. Tsai, 'Modeling Alzheimer's disease with iPSC-derived brain cells', *Mol. Psychiatry*, vol. 25, no. 1, pp. 148–167, 2020, doi: 10.1038/s41380-019-0468-3.
[18] S. Absalon, D. M. Kochanek, V. Raghavan, and A. M. Krichevsky, 'MiR-26b, upregulated in Alzheimer's disease, activates cell cycle entry, tau-phosphorylation, and apoptosis in postmitotic neurons', *J. Neurosci. Off. J. Soc. Neurosci.*, vol. 33, no. 37, pp. 14645–14659, Sep. 2013, doi: 10.1523/JNEUROSCI.1327-13.2013.
[19] J. Chen, Y. Qi, C.-F. Liu, J.-M. Lu, J. Shi, and Y. Shi, 'MicroRNA expression data analysis to identify key miRNAs associated with Alzheimer's disease', *J. Gene Med.*, vol. 20, no. 6, p. e3014, Jun. 2018, doi: 10.1002/jgm.3014.
[20] A. Turk, T. Kunej, and B. Peterlin, 'MicroRNA-Target Interaction Regulatory Network in Alzheimer's Disease', *J. Pers. Med.*, vol. 11, no. 12, p. 1275, Dec. 2021, doi: 10.3390/jpm11121275.
[21] S. C. Ribeiro, R. Fernandes, F. T. C. Moreira, and M. G. F. Sales, 'Potentiometric Biosensor Based on Artificial Antibodies for an Alzheimer Biomarker Detection', *Appl. Sci.*, vol. 12, no. 7, Art. no. 7, Jan. 2022, doi: 10.3390/app12073625.
[22] C. A. Lane, J. Hardy, and J. M. Schott, 'Alzheimer's disease', *Eur. J. Neurol.*, vol. 25, no. 1, pp. 59–70, Jan. 2018, doi: 10.1111/ene.13439.
[23] M. J. Millan, 'Linking deregulation of non-coding RNA to the core pathophysiology of Alzheimer's disease: An integrative review', *Prog. Neurobiol.*, vol. 156, pp. 1–68, Sep. 2017, doi: 10.1016/j.pneurobio.2017.03.004.
[24] M. Cosín-Tomás *et al.*, 'Plasma miR-34a-5p and miR-545-3p as Early Biomarkers of Alzheimer's Disease: Potential and Limitations', *Mol. Neurobiol.*, vol. 54, no. 7, pp. 5550–5562, Sep. 2017, doi: 10.1007/s12035-016-0088-8.
[25] P. Chen, F. Chen, J. Lei, Q. Li, and B. Zhou, 'Activation of the miR-34a-Mediated SIRT1/mTOR Signaling Pathway by Urolithin A Attenuates D-Galactose-Induced Brain Aging in Mice', *Neurother. J. Am. Soc. Exp. Neurother.*, vol. 16, no. 4, pp. 1269–1282, Oct. 2019, doi: 10.1007/s13311-019-00753-0.
[26] S. Sarkar *et al.*, 'Over-expression of miR-34a induces rapid cognitive impairment and Alzheimer's disease-like pathology', *Brain Res.*, vol. 1721, p. 146327, Oct. 2019, doi: 10.1016/j.brainres.2019.146327.
[27] M. Samadian, M. Gholipour, M. Hajiesmaeili, M. Taheri, and S. Ghafouri-Fard, 'The Eminent Role of microRNAs in the Pathogenesis of Alzheimer's Disease', *Front. Aging Neurosci.*, vol. 13, 2021, Accessed: Jul. 01, 2022. [Online]. Available: https://www.frontiersin.org/article/10.3389/fnagi.2021.641080
[28] D. Wakhloo, J. Oberhauser, A. Madira, and S. Mahajani, 'From cradle to grave: neurogenesis, neuroregeneration and neurodegeneration in Alzheimer's and Parkinson's diseases', *Neural Regen. Res.*, vol. 17, no. 12, pp. 2606–2614, Dec. 2022, doi: 10.4103/1673-5374.336138.
[29] S. Swarbrick, N. Wragg, S. Ghosh, and A. Stolzing, 'Systematic Review of miRNA as Biomarkers in Alzheimer's Disease', *Mol. Neurobiol.*, vol. 56, no. 9, pp. 6156–6167, Sep. 2019, doi: 10.1007/s12035-019-1500-y.
[30] H. Braak and E. Braak, 'Staging of Alzheimer's disease-related neurofibrillary changes', *Neurobiol. Aging*, vol. 16, no. 3, pp. 271–278; discussion 278-284, Jun. 1995, doi: 10.1016/0197-4580(95)00021-6.
[31] A. Nunomura and G. Perry, 'RNA and Oxidative Stress in Alzheimer's Disease: Focus on microRNAs', *Oxid. Med. Cell. Longev.*, vol. 2020, p. 2638130, Nov. 2020, doi: 10.1155/2020/2638130.
[32] S. Sarkar, S. Jun, S. Rellick, D. D. Quintana, J. Z. Cavendish, and J. W. Simpkins, 'Expression of microRNA-34a in Alzheimer's disease brain targets genes linked to synaptic plasticity, energy metabolism, and resting state network activity', *Brain Res.*, vol. 1646, pp. 139–151, Sep. 2016, doi: 10.1016/j.brainres.2016.05.026.

[33] S. Cetin, D. Knez, S. Gobec, J. Kos, and A. Pišlar, 'Cell models for Alzheimer's and Parkinson's disease: At the interface of biology and drug discovery', *Biomed. Pharmacother.*, vol. 149, p. 112924, May 2022, doi: 10.1016/j.biopha.2022.112924.
[34] Center for Drug Evaluation and Research, 'Aducanumab (marketed as Aduhelm) Information', *FDA*, Aug. 07, 2021. https://www.fda.gov/drugs/postmarket-drug-safety-information-patients-and-providers/aducanumab-marketed-aduhelm-information (accessed Aug. 08, 2022).
[35] Z. Song *et al.*, 'Microarray microRNA profiling of urinary exosomes in a 5XFAD mouse model of Alzheimer's disease', *Anim. Models Exp. Med.*, vol. 4, no. 3, pp. 233–242, 2021, doi: 10.1002/ame2.12175.
[36] I. C. Fontana *et al.*, 'Amyloid-ß oligomers in cellular models of Alzheimer's disease', *J. Neurochem.*, vol. 155, no. 4, pp. 348–369, 2020, doi: 10.1111/jnc.15030.
[37] European Collection of Cell Cultures, 'ECACC General Cell Collection: SH-SY5Y'. https://www.culturecollections.org.uk/products/celllines/generalcell/detail.jsp?refId=94030304&collection=ecacc_gc (accessed Jul. 01, 2022).
[38] Z. Xun *et al.*, 'Retinoic acid-induced differentiation increases the rate of oxygen consumption and enhances the spare respiratory capacity of mitochondria in SH-SY5Y cells', *Mech. Ageing Dev.*, vol. 133, no. 4, pp. 176–185, Apr. 2012, doi: 10.1016/j.mad.2012.01.008.
[39] AcceGen R&D Team, 'SH-SY5Y Cell Line Culture Protocol and Research Applications'. https://www.accegen.com/recent-posts/sh-sy5y-cell-line-culture-protocol-and-research-applications/ (accessed Sep. 14, 2022).
[40] J. R. Murillo, L. Goto-Silva, A. Sánchez, F. C. S. Nogueira, G. B. Domont, and M. Junqueira, 'Quantitative proteomic analysis identifies proteins and pathways related to neuronal development in differentiated SH-SY5Y neuroblastoma cells', *EuPA Open Proteomics*, vol. 16, pp. 1–11, Sep. 2017, doi: 10.1016/j.euprot.2017.06.001.
[41] R. F. Simões *et al.*, 'Refinement of a differentiation protocol using neuroblastoma SH-SY5Y cells for use in neurotoxicology research', *Food Chem. Toxicol.*, vol. 149, p. 111967, Mar. 2021, doi: 10.1016/j.fct.2021.111967.
[42] M. Gomez-Lazaro, N. A. Bonekamp, M. F. Galindo, J. Jordán, and M. Schrader, '6-Hydroxydopamine (6-OHDA) induces Drp1-dependent mitochondrial fragmentation in SH-SY5Y cells', *Free Radic. Biol. Med.*, vol. 44, no. 11, pp. 1960–1969, Jun. 2008, doi: 10.1016/j.freeradbiomed.2008.03.009.
[43] M. Ahmadzadeh-Darinsoo, M. Ahmadzadeh-Darinsoo, S. Abbasi, E. Arefian, C. Bernard, and A. P. Tafreshi, 'Altered expression of miR-29a-3p and miR-34a-5p by specific inhibition of GSK3ß in the MPP+ treated SH-SY5Y Parkinson's model', *Non-Coding RNA Res.*, vol. 7, no. 1, pp. 1–6, Mar. 2022, doi: 10.1016/j.ncrna.2021.12.004.
[44] Q. Ba, C. Cui, L. Wen, S. Feng, J. Zhou, and K. Yang, 'Schisandrin B shows neuroprotective effect in 6-OHDA-induced Parkinson's disease via inhibiting the negative modulation of miR-34a on Nrf2 pathway', *Biomed. Pharmacother.*, vol. 75, pp. 165–172, Oct. 2015, doi: 10.1016/j.biopha.2015.07.034.
[45] Z. Shanesazzade, M. Peymani, K. Ghaedi, and M. H. Nasr Esfahani, 'miR-34a/BCL-2 signaling axis contributes to apoptosis in MPP+-induced SH-SY5Y cells', *Mol. Genet. Genomic Med.*, vol. 6, no. 6, pp. 975–981, 2018, doi: 10.1002/mgg3.469.
[46] L. Cheng *et al.*, 'Prognostic serum miRNA biomarkers associated with Alzheimer's disease shows concordance with neuropsychological and neuroimaging assessment', *Mol. Psychiatry*, vol. 20, no. 10, pp. 1188–1196, Oct. 2015, doi: 10.1038/mp.2014.127.
[47] I. Maldonado-Lasuncion, M. Atienza, M. P. Sanchez-Espinosa, and J. L. Cantero, 'Aging-Related Changes in Cognition and Cortical Integrity are Associated With Serum Expression of Candidate MicroRNAs for Alzheimer Disease', *Cereb. Cortex N. Y. N 1991*, vol. 29, no. 10, pp. 4426–4437, Sep. 2019, doi: 10.1093/cercor/bhy323.
[48] M. Eduarda Schneider, L. Guillade, M. A. Correa-Duarte, and F. T. C. Moreira, 'Development of a biosensor for phosphorylated Tau 181 protein detection in Early-Stage Alzheimer's disease', *Bioelectrochemistry*, vol. 145, p. 108057, Jun. 2022, doi: 10.1016/j.bioelechem.2022.108057.
[49] A. R. Cardoso, F. T. C. Moreira, R. Fernandes, and M. G. F. Sales, 'Novel and simple electrochemical biosensor monitoring attomolar levels of miRNA-155 in breast cancer', *Biosens. Bioelectron.*, vol. 80, pp. 621–630, Jun. 2016, doi: 10.1016/j.bios.2016.02.035.

[50] E. Kesici, E. Eksin, and A. Erdem, 'An Impedimetric Biosensor Based on Ionic Liquid-Modified Graphite Electrodes Developed for microRNA-34a Detection', *Sensors*, vol. 18, no. 9, Art. no. 9, Sep. 2018, doi: 10.3390/s18092868.
[51] V. M. Serrano, I. S. P. Silva, A. R. Cardoso, and M. G. F. Sales, 'Carbon Electrodes with Gold Nanoparticles for the Electrochemical Detection of miRNA 21-5p', *Chemosensors*, vol. 10, no. 5, Art. no. 5, May 2022, doi: 10.3390/chemosensors10050189.
[52] C. Jian *et al.*, 'miR-34a knockout attenuates cognitive deficits in APP/PS1 mice through inhibition of the amyloidogenic processing of APP', *Life Sci.*, vol. 182, pp. 104–111, Aug. 2017, doi: 10.1016/j.lfs.2017.05.023.
[53] Y. Wu, Q. Li, R. Zhang, X. Dai, W. Chen, and D. Xing, 'Circulating microRNAs: Biomarkers of disease', *Clin. Chim. Acta*, vol. 516, pp. 46–54, May 2021, doi: 10.1016/j.cca.2021.01.008.
[54] N. Tong, R. Jin, Z. Zhou, and X. Wu, 'Involvement of microRNA-34a in Age-Related Susceptibility to Oxidative Stress in ARPE-19 Cells by Targeting the Silent Mating Type Information Regulation 2 Homolog 1/p66shc Pathway: Implications for Age-Related Macular Degeneration', *Front. Aging Neurosci.*, vol. 11, p. 137, 2019, doi: 10.3389/fnagi.2019.00137.
[55] P. Takousis *et al.*, 'Differential expression of microRNAs in Alzheimer's disease brain, blood, and cerebrospinal fluid', *Alzheimers Dement.*, vol. 15, no. 11, pp. 1468–1477, 2019, doi: 10.1016/j.jalz.2019.06.4952.
[56] X. Li, A. Khanna, N. Li, and E. Wang, 'Circulatory miR34a as an RNAbased, noninvasive biomarker for brain aging', *Aging*, vol. 3, no. 10, pp. 985–1002, Oct. 2011, doi: 10.18632/aging.100371.
[57] G. Congur, E. Eksin, and A. Erdem, 'Impedimetric Detection of microRNA at Graphene Oxide Modified Sensors', *Electrochimica Acta*, vol. 172, pp. 20–27, agosto 2015, doi: 10.1016/j.electacta.2015.03.210.
[58] Y. Ma *et al.*, 'MicroRNA-34a Mediates the Autocrine Signaling of PAR2-Activating Proteinase and Its Role in Colonic Cancer Cell Proliferation', *PLOS ONE*, vol. 8, no. 8, p. e72383, Aug. 2013, doi: 10.1371/journal.pone.0072383.
[59] P. K. Modi, S. Jaiswal, and P. Sharma, 'Regulation of Neuronal Cell Cycle and Apoptosis by MicroRNA 34a', *Mol. Cell. Biol.*, vol. 36, no. 1, pp. 84–94, Jan. 2016, doi: 10.1128/MCB.00589-15.
[60] A. Turchinovich, L. Weiz, A. Langheinz, and B. Burwinkel, 'Characterization of extracellular circulating microRNA', *Nucleic Acids Res.*, vol. 39, no. 16, pp. 7223–7233, Sep. 2011, doi: 10.1093/nar/gkr254.
[61] N. Vigneron *et al.*, 'Towards a new standardized method for circulating miRNAs profiling in clinical studies: Interest of the exogenous normalization to improve miRNA signature accuracy', *Mol. Oncol.*, vol. 10, no. 7, pp. 981–992, Aug. 2016, doi: 10.1016/j.molonc.2016.03.005.
[62] C. E. L. Chua and B. L. Tang, 'miR-34a in Neurophysiology and Neuropathology', *J. Mol. Neurosci.*, vol. 67, no. 2, pp. 235–246, Feb. 2019, doi: 10.1007/s12031-018-1231-y.
[63] X. Wang *et al.*, 'miR-34a, a microRNA up-regulated in a double transgenic mouse model of Alzheimer's disease, inhibits bcl2 translation', *Brain Res. Bull.*, vol. 80, no. 4–5, pp. 268–273, Oct. 2009, doi: 10.1016/j.brainresbull.2009.08.006.
[64] S. Mao, Q. Sun, H. Xiao, C. Zhang, and L. Li, 'Secreted miR-34a in astrocytic shedding vesicles enhanced the vulnerability of dopaminergic neurons to neurotoxins by targeting Bcl-2', *Protein Cell*, vol. 6, no. 7, pp. 529–540, Jul. 2015, doi: 10.1007/s13238-015-0168-y.
[65] M. C. Gao *et al.*, 'Intelligence in Williams Syndrome Is Related to STX1A, Which Encodes a Component of the Presynaptic SNARE Complex', *PLoS ONE*, vol. 5, no. 4, p. e10292, Apr. 2010, doi: 10.1371/journal.pone.0010292.
[66] Z. Shi *et al.*, 'Increased miR-34c mediates synaptic deficits by targeting synaptotagmin 1 through ROS-JNK-p53 pathway in Alzheimer's Disease', *Aging Cell*, vol. 19, no. 3, p. e13125, Mar. 2020, doi: 10.1111/acel.13125.
[67] J. P. Cogswell *et al.*, 'Identification of miRNA changes in Alzheimer's disease brain and CSF yields putative biomarkers and insights into disease pathways', *J. Alzheimers Dis.*, vol. 14, no. 1, pp. 27–41, May 2008, doi: 10.3233/jad-2008-14103.

[68] A. Koyappayil and M.-H. Lee, 'Ultrasensitive Materials for Electrochemical Biosensor Labels', *Sensors*, vol. 21, no. 1, p. 89, Dec. 2020, doi: 10.3390/s21010089.
[69] A. Singh *et al.*, 'Recent Advances in Electrochemical Biosensors: Applications, Challenges, and Future Scope', *Biosensors*, vol. 11, no. 9, p. 336, Sep. 2021, doi: 10.3390/bios11090336.
[70] H. S. Magar, R. Y. A. Hassan, and A. Mulchandani, 'Electrochemical Impedance Spectroscopy (EIS): Principles, Construction, and Biosensing Applications', *Sensors*, vol. 21, no. 19, p. 6578, Oct. 2021, doi: 10.3390/s21196578.
[71] M. C. C. G. Carneiro, F. T. C. Moreira, R. A. F. Dutra, R. Fernandes, and M. G. F. Sales, 'Homemade 3-carbon electrode system for electrochemical sensing: Application to microRNA detection', *Microchem. J.*, vol. 138, pp. 35–44, maio 2018, doi: 10.1016/j.microc.2017.12.026.
[72] V. Mirceski, S. Skrzypek, and L. Stojanov, 'Square-wave voltammetry', *ChemTexts*, vol. 4, no. 4, p. 17, Nov. 2018, doi: 10.1007/s40828-018-0073-0.
[73] L. C. Brazaca *et al.*, 'Electrochemical immunosensors using electrodeposited gold nanostructures for detecting the S proteins from SARS-CoV and SARS-CoV-2', *Anal. Bioanal. Chem.*, vol. 414, no. 18, pp. 5507–5517, Jul. 2022, doi: 10.1007/s00216-022-03956-1.
[74] N. Elgrishi, K. J. Rountree, B. D. McCarthy, E. S. Rountree, T. T. Eisenhart, and J. L. Dempsey, 'A Practical Beginner's Guide to Cyclic Voltammetry', *J. Chem. Educ.*, vol. 95, no. 2, pp. 197–206, Feb. 2018, doi: 10.1021/acs.jchemed.7b00361.
[75] G. Maduraiveeran and W. Jin, 'Nanomaterials based electrochemical sensor and biosensor platforms for environmental applications', *Trends Environ. Anal. Chem.*, vol. 13, pp. 10–23, Jan. 2017, doi: 10.1016/j.teac.2017.02.001.
[76] A. Blidar, O. Hosu, B. Feier, G. Ştefan, D. Bogdan, and C. Cristea, 'Gold-based nanostructured platforms for oxytetracycline detection from milk by a "signal-on" aptasensing approach', *Food Chem.*, vol. 371, p. 131127, Mar. 2022, doi: 10.1016/j.foodchem.2021.131127.
[77] C.-H. Chen and S.-C. Luo, 'Tuning Surface Charge and Morphology for the Efficient Detection of Dopamine under the Interferences of Uric Acid, Ascorbic Acid, and Protein Adsorption', *ACS Appl. Mater. Interfaces*, vol. 7, no. 39, pp. 21931–21938, Oct. 2015, doi: 10.1021/acsami.5b06526.
[78] C. M. A. Brett, 'Electrochemical Impedance Spectroscopy in the Characterisation and Application of Modified Electrodes for Electrochemical Sensors and Biosensors', *Molecules*, vol. 27, no. 5, Art. no. 5, Jan. 2022, doi: 10.3390/molecules27051497.
[79] G. Instruments, 'Basics of electrochemical impedance spectroscopy', *G Instrum. Complex Impedance Corros.*, pp. 1–30, 2007.
[80] G. Congur and A. Erdem, 'PAMAM dendrimer modified screen printed electrodes for impedimetric detection of miRNA-34a', *Microchem. J.*, vol. 148, pp. 748–758, Jul. 2019, doi: 10.1016/j.microc.2019.05.040.
[81] C.-H. Lin, C.-C. Wu, and Y.-F. Kuo, 'A high sensitive impedimetric salbutamol immunosensor based on the gold nanostructure-deposited screen-printed carbon electrode', *J. Electroanal. Chem.*, vol. 768, pp. 27–33, May 2016, doi: 10.1016/j.jelechem.2016.02.036.
[82] E. Boisselier and D. Astruc, 'Gold nanoparticles in nanomedicine: preparations, imaging, diagnostics, therapies and toxicity', *Chem. Soc. Rev.*, vol. 38, no. 6, pp. 1759–1782, May 2009, doi: 10.1039/B806051G.
[83] J. Pryjmaková, M. Kaimlová, T. Hubáček, V. Švorčík, and J. Siegel, 'Nanostructured Materials for Artificial Tissue Replacements', *Int. J. Mol. Sci.*, vol. 21, no. 7, p. 2521, Apr. 2020, doi: 10.3390/ijms21072521.
[84] B. R. Smith and S. S. Gambhir, 'Nanomaterials for In Vivo Imaging', *Chem. Rev.*, vol. 117, no. 3, pp. 901–986, Feb. 2017, doi: 10.1021/acs.chemrev.6b00073.
[85] M. Jiao *et al.*, 'Recent advancements in biocompatible inorganic nanoparticles towards biomedical applications', *Biomater. Sci.*, vol. 6, no. 4, pp. 726–745, Mar. 2018, doi: 10.1039/C7BM01020F.
[86] Z. Ma, T. Song, Y. Yuan, and Y. Yang, 'Synergistic catalysis on Fe–Nx sites and Fe nanoparticles for efficient synthesis of quinolines and quinazolinones via oxidative

coupling of amines and aldehydes', *Chem. Sci.*, vol. 10, no. 44, pp. 10283–10289, Nov. 2019, doi: 10.1039/C9SC04060A.
[87] Z. Gao *et al.*, 'Small is Smarter: Nano MRI Contrast Agents – Advantages and Recent Achievements', *Small*, vol. 12, no. 5, pp. 556–576, 2016, doi: 10.1002/smll.201502309.
[88] G. Maduraiveeran, M. Sasidharan, and V. Ganesan, 'Electrochemical sensor and biosensor platforms based on advanced nanomaterials for biological and biomedical applications', *Biosens. Bioelectron.*, vol. 103, pp. 113–129, Apr. 2018, doi: 10.1016/j.bios.2017.12.031.
[89] K. Y. Goud *et al.*, 'Progress on nanostructured electrochemical sensors and their recognition elements for detection of mycotoxins: A review', *Biosens. Bioelectron.*, vol. 121, pp. 205–222, Dec. 2018, doi: 10.1016/j.bios.2018.08.029.
[90] T. Xiao, J. Huang, D. Wang, T. Meng, and X. Yang, 'Au and Au-Based nanomaterials: Synthesis and recent progress in electrochemical sensor applications', *Talanta*, vol. 206, p. 120210, Jan. 2020, doi: 10.1016/j.talanta.2019.120210.
[91] A. Blidar, B. Feier, A. Pusta, A.-M. Drăgan, and C. Cristea, 'Graphene–Gold Nanostructures Hybrid Composites Screen-Printed Electrode for the Sensitive Electrochemical Detection of Vancomycin', *Coatings*, vol. 9, no. 10, Art. no. 10, Oct. 2019, doi: 10.3390/coatings9100652.
[92] C. Hou, Q. Luo, Y. He, and H. Zhang, 'Potentiostatic electrodeposition of gold nanoparticles: variation of electrocatalytic activity toward four targets', *J. Appl. Electrochem.*, vol. 51, no. 12, pp. 1721–1730, Dec. 2021, doi: 10.1007/s10800-021-01604-7.
[93] J. Thangphatthanarungruang, C. Chotsuwan, S. Jampasa, and W. Siangproh, 'A new nanocomposite-based screen-printed graphene electrode for sensitive and selective detection of 8-hydroxy-2′-deoxyguanosine', *FlatChem*, vol. 32, p. 100335, Mar. 2022, doi: 10.1016/j.flatc.2022.100335.
[94] W. Lipińska, K. Grochowska, and K. Siuzdak, 'Enzyme Immobilization on Gold Nanoparticles for Electrochemical Glucose Biosensors', *Nanomaterials*, vol. 11, no. 5, p. 1156, Apr. 2021, doi: 10.3390/nano11051156.
[95] W.-R. Zhao, T.-F. Kang, L.-P. Lu, F.-X. Shen, and S.-Y. Cheng, 'A novel electrochemical sensor based on gold nanoparticles and molecularly imprinted polymer with binary functional monomers for sensitive detection of bisphenol A', *J. Electroanal. Chem.*, vol. 786, pp. 102–111, Feb. 2017, doi: 10.1016/j.jelechem.2017.01.003.
[96] H.-A. Rafiee-Pour, M. Behpour, and M. Keshavarz, 'A novel label-free electrochemical miRNA biosensor using methylene blue as redox indicator: application to breast cancer biomarker miRNA-21', *Biosens. Bioelectron.*, vol. 77, pp. 202–207, Mar. 2016, doi: 10.1016/j.bios.2015.09.025.
[97] V. Vanova, E. Sedlackova, D. Hynek, L. Richtera, Z. Bytesnikova, and V. Adam, 'Highly selective and sensitive electrochemical biosensor based on electrochemically reduced graphene oxide for detection of mirna as a cancer biomarker', 2020, vol. 2020-October, pp. 385–390. doi: 10.37904/nanocon.2019.8615.
[98] A. Bharti, S. Mittal, S. Rana, D. Dahiya, N. Agnihotri, and N. Prabhakar, 'Electrochemical biosensor for miRNA-21 based on gold-platinum bimetallic nanoparticles coated 3-aminopropyltriethoxy silane', *Anal. Biochem.*, vol. 609, p. 113908, Nov. 2020, doi: 10.1016/j.ab.2020.113908.
[99] J. Mandli and A. Amine, 'Impedimetric genosensor for miRNA-34a detection in cell lysates using polypyrrole', *J. Solid State Electrochem.*, vol. 22, no. 4, pp. 1007–1014, Apr. 2018, doi: 10.1007/s10008-017-3819-5.
[100] F. T. C. Moreira, M. G. F. Sale, and M. Di Lorenzo, 'Towards timely Alzheimer diagnosis: A self-powered amperometric biosensor for the neurotransmitter acetylcholine', *Biosens. Bioelectron.*, vol. 87, pp. 607–614, Jan. 2017, doi: 10.1016/j.bios.2016.08.104.
[101] Metrohm DropSens, 'Metrohm DropSens: Screen-Printed electrodes'. https://www.dropsens.com/en/screen_printed_electrodes_pag.html (accessed Sep. 07, 2022).
[102] '3-Mercaptopropionic acid', *Wikipedia*. Nov. 17, 2021. Accessed: Aug. 17, 2022. [Online]. Available: https://en.wikipedia.org/w/index.php?title=3-Mercaptopropionic_acid&oldid=1055674692

[103] ThermoFisher Scientific, ‘Carbodiimide Crosslinker Chemistry’. https://www.thermofisher.com/uk/en/home/life-science/protein-biology/protein-biology-learning-center/protein-biology-resource-library/pierce-protein-methods/carbodiimide-crosslinker-chemistry.html (accessed Sep. 05, 2022).
[104] A. Kolodziej, F. Fernandez-Trillo, and P. Rodriguez, ‘Determining the parameters governing the electrochemical stability of thiols and disulfides self-assembled monolayer on gold electrodes in physiological medium’, *J. Electroanal. Chem.*, vol. 819, pp. 51–57, Jun. 2018, doi: 10.1016/j.jelechem.2017.07.039.
[105] K. L. Wong and J. Liu, ‘Factors and methods to modulate DNA hybridization kinetics’, *Biotechnol. J.*, vol. 16, no. 11, p. 2000338, 2021, doi: 10.1002/biot.202000338.
[106] H. Ravan, S. Kashanian, N. Sanadgol, A. Badoei-Dalfard, and Z. Karami, ‘Strategies for optimizing DNA hybridization on surfaces’, *Anal. Biochem.*, vol. 444, pp. 41–46, Jan. 2014, doi: 10.1016/j.ab.2013.09.032.
[107] R. Cánovas, M. Cuartero, and G. A. Crespo, ‘Modern creatinine (Bio)sensing: Challenges of point-of-care platforms’, *Biosens. Bioelectron.*, vol. 130, pp. 110–124, Apr. 2019, doi: 10.1016/j.bios.2019.01.048.
[108] S. Ghavami *et al.*, ‘Autophagy and apoptosis dysfunction in neurodegenerative disorders’, *Prog. Neurobiol.*, vol. 112, pp. 24–49, Jan. 2014, doi: 10.1016/j.pneurobio.2013.10.004.
[109] P. Tanapat, ‘Neuronal Cell Markers’, *Mater. Methods*, Jun. 2022, doi: //dx.doi.org/10.13070/mm.en.3.196.
[110] S. C. H. Rehfeldt *et al.*, ‘Neuroprotective Effect of Luteolin-7-O-Glucoside against 6-OHDA-Induced Damage in Undifferentiated and RA-Differentiated SH-SY5Y Cells’, *Int. J. Mol. Sci.*, vol. 23, no. 6, Art. no. 6, Jan. 2022, doi: 10.3390/ijms23062914.
[111] ThermoFisher Scientific, ‘TaqMan™ MicroRNA Reverse Transcription Kit’. https://www.thermofisher.com/order/catalog/product/4366596 (accessed Sep. 07, 2022).
[112] ThermoFisher Scientific, ‘TaqMan™ MicroRNA Assays and Arrays’. https://www.thermofisher.com/document-connect/document-connect.html?url=https://assets.thermofisher.com/TFS-Assets%2FLSG%2Fbrochures%2Fcms_042142.pdf (accessed Sep. 07, 2022).

Annex – Alternative biosensor designs

This annex summarizes the alternative designs tested for the biosensor that failed to detect miR-34a. The foundation of these designs were C-SPEs electrodes pre-treated by CA (1.6 V for 200 s) with 70 µL of a 0.1 M KCl solution. The pre-treated electrodes were then modified with a polymer film, according to the following table.

Polymer solution	Electropolymerizing condition
10 mM Thiophene-COOH	CA (1.0 V potential for 10 s)
	4 consecutive CVs (ranging from -0.4 to +0.7 V, using a scan rate of 50 mV/s)
10 mM EDOT	CA (1.0 V potential for 10 s)
10 mM EDOT + 10 mM Thiophene-COOH	CA (1.0 V potential for 10 s)
3 mM EDOT + 10 mM Pyrrole-COOH	1 CV (ranging from -0.4 to +1.0 V, using a scan rate of 50 mV/s)
5 mM EDOT + 10 mM Pyrrole-COOH	
10 mM EDOT + 10 mM Pyrrole-COOH	

Thiophene-COOH: 3-thiophenecarboxylic acid; EDOT: 3,4-ethylenedioxytiophene; Pyrrole-COOH: pyrrole-2-carboxylic acid).

After electropolymerizing the polymer on the surface of the sensor, the carboxylic groups of the polymer were activated through an EDAC/NHS reaction and the anti-miR-34a was bound to the surface. Then, the sensor was calibrated using miR-34a standard solutions of rising concentrations. These steps were performed as described on Chapter 2.